

**University of Alberta**

Magneto-resistance Effects in Carbon-Based Nanostructures

by

Abhay Pratap Singh

A thesis submitted to the Faculty of Graduate Studies and Research  
in partial fulfillment of the requirements for the degree of

Master of Science

in

Microsystems and Nanodevices

Department of Electrical and Computer Engineering

©Abhay Pratap Singh

Spring 2014

Edmonton, Alberta

Permission is hereby granted to the University of Alberta Libraries to reproduce single copies of this thesis and to lend or sell such copies for private, scholarly or scientific research purposes only. Where the thesis is converted to, or otherwise made available in digital form, the University of Alberta will advise potential users of the thesis of these terms.

The author reserves all other publication and other rights in association with the copyright in the thesis and, except as herein before provided, neither the thesis nor any substantial portion thereof may be printed or otherwise reproduced in any material form whatsoever without the author's prior written permission

## **Abstract**

Magnetoresistance (MR) effect is extensively used in state-of-the-art magnetic field sensing and data storage devices. In this work, we present (a) current-perpendicular-to-plane (CPP) MR effect in multilayer graphene (MLG) grown on cobalt (Co) foil and (b) spin valve MR effect in a vertical array of multiwall carbon nanotube (MWCNT) spin valves. In part (a) strong room-temperature CPP-MR effects have been observed in as-grown MLG on Co. The origin of the MR effect lies in the graphene-Co interface and interlayer coupling between the graphene layers of MLG. In part (b) an array of vertically standing MWCNT spin valves has been synthesized in the pores of an anodic alumina template. A spin valve MR and spin relaxation length of  $\sim 0.28 \mu\text{m}$  have been observed at 8 K, which disappears at higher temperature. This indicates necessity of alternative designs for room temperature operation of MWCNT spin valves.

## **Acknowledgment**

I express my deep sense of gratitude and indebtedness to my supervisor Dr. Sandipan Pramanik, without whose inspiring guidance and consistent interest, this project was a virtual chimera for me. It has been a memorable, everlasting experience for me to work with his benign presence and guidance. It is impossible for me to bind my reverence for him in words. I also express my sincere obligation to Department of Electrical and Computer Engineering, TRLab (now known as TRTech) and NSERC for providing continuous financial support.

I also owe a lot to Mr. Mike O'toole, Rob Indoe, and Tim Patrie (Clean Room, National Institute for Nanotechnology (NINT), University of Alberta) for training of the clean room equipment and Mr. Mike Xia (Organic/Inorganic Analytical Lab at NINT) for training me to operate Raman system and providing valuable help during its operation. I would like to thank De-ann Rollings (Earth and Atmospheric Sciences Department, University of Alberta) for help in acquiring FESEM images and Shiraz Merali (Chemical and Materials Engineering, University of Alberta) for help in XRD characterization. I would like to thank both Shiau-Yin Wu (Integrated Nanosystems Research Facility (INRF), University of Alberta) and Shihong Xu (Alberta Center for Surface Engineering and Science (ACSES), University of Alberta) for help in Atomic Force Microscopy (AFM) operation. I am grateful for Collin Twanow (nanoFAB, University of Alberta) for all the training and teaching experience during the Microfabrication lab in nanoFAB. I would like to thank all my research group members Kazi Alam, Chanakya Bodepudi, and Ryan Starko-Bowes for their continued cooperation during whole project work. I express my honest goodwill for all my colleagues at the University of Alberta for their sincere endeavors during my project work. Last but not the least I would like to pay my sincere tribute to almighty, my beloved parents and family whose spiritual omnipresence was an inspiring factor to carry on all this work to a satisfactory conclusion.

# Table of Contents

1	Introduction.....	1
1.1	Magnetoresistance (MR) Effects in Graphene and Carbon Nanotubes (CNTs)1	
1.1.1	Spin-Dependent MR Effects in Graphene and CNT.....	2
1.1.2	Spin-Independent MR Effects in Graphene and CNT .....	4
1.2	Chemical Vapor Deposition Growth of Graphene and CNT .....	5
1.3	Raman Spectroscopy of Carbon Nanotubes and Graphene .....	7
1.4	Motivation of This Work .....	9
1.5	Work Completed to Date .....	10
1.5.1	Magnetoresistance Effects in As-Grown MLG on Co Foil .....	10
1.5.2	Spin Valve Effect in High Density Array of Multi-Walled Carbon Nanotubes .....	11
1.6	Future Work.....	11
2	Experimental Study of c-axis MR in Multilayer Graphene as-Grown on Co Foil ...	12
2.1	Introduction.....	12
2.2	Experimental Methods .....	16
2.2.1	Growth of MLG on Cobalt (Co) Foil.....	16
2.2.2	Device Fabrication: Process Flow .....	17
2.2.3	Raman Spectroscopy of MLG As-Grown on Co .....	19
2.2.4	MLG/Co Surface Morphology and Step Height Measurement Using Atomic Force Microscopy (AFM) .....	23
2.2.5	Device Structure .....	24
2.2.6	CPP MR Measurements on As-Grown MLG/Co .....	25
2.2.7	CPP MR of Transferred MLG on Gold (Au) electrode .....	29
2.2.8	Current-in-Plane (CIP) MR of Transferred MLG on Glass Substrate	30
2.3	Result and Discussion .....	31
2.4	Conclusion .....	32
3	High Density Integration of MWCNT Spin Valves .....	33
3.1	Introduction.....	33
3.2	Experimental Methods .....	34
3.2.1	Fabrication of Nanoporous Anodic Aluminum Oxide (AAO) Template .....	34
3.2.2	Fabrication of Spin Valve Using MWCNT as Spacer Layer .....	36
3.2.3	Characterization of MWCNT Using Raman Spectroscopy .....	39

3.2.4	Spin-valve Characterization.....	39
3.3	Result and Discussion.....	39
3.4	Conclusion .....	42
4	Summary and Outlook.....	44
	References.....	46

## List of Figures

Figure 1.1 Schematic of a spin valve response. ....	3
Figure 1.2 Different methods of producing large-scale graphene. CVD allows growth of high quality graphene at a low cost (taken from ref. [11]).....	6
Figure 1.3 Raman scattering process (not drawn to scale), left panel showing Stokes process and the right panel is Anti-Stokes process (adapted from ref. [68]). ....	7
Figure 1.4 CNT applications in microelectronics. (A) Flexible TFTs using CNT networks deposited by aerosol CVD. (B) CNT-based nonvolatile random access memory (NRAM) cell (C) CMOS-compatible 150-nm vertical interconnects (D) CNT bumps used for enhanced thermal dissipation in high power amplifiers. (taken from reference [71]). ....	8
Figure 2.1 Field emission scanning electron microscope (FESEM) image of (a), (b) bare Cobalt (Co) foil and (c), (d) as grown multilayer (MLG) graphene on Co foil at different magnifications.....	16
Figure 2.2 XRD spectrum of as-purchased Co foil (from Alfa Aesar). Presence of several peaks indicates the polycrystalline nature of the Co foil. ....	17
Figure 2.3 Schematic diagram of MLG growth and transfer on arbitrary substrate. ....	18
Figure 2.4 Optical image of as-grown MLG on Co foil. Top half of the sample is protected and the bottom half is exposed to O <sub>2</sub> plasma etching.....	19
Figure 2.5 Representative Raman spectra of as-grown MLG on Co foil (a) $I_{2D} > I_G$ and 2D peak is symmetrical (b) $I_{2D} < I_G$ and 2D is still symmetrical (c) $I_{2D} < I_G$ and 2D shows HOPG-like shoulder (d) $I_{2D} < I_G$ and 2D peak ( $\sim 2685 \text{ cm}^{-1} - 2720 \text{ cm}^{-1}$ ) is split into sub-peaks. ....	20
Figure 2.6 (a) Optical image of highly oriented pyrolytic graphite (HOPG as acquired from SPI supplies). (b) Raman spectrum of HOPG. The inset shows the 2D band which can be fit by two Lorentzians.....	22
Figure 2.7 (a) Optical image of MLG/Co surface (b) HOPG like Raman spectrum of MLG/Co sample, inset showing 2D band with two Lorentzian fitting.....	22
Figure 2.8 3D Atomic force microscopy (AFM) surface morphology of as-grown epitaxial MLG on Co foil.....	23
Figure 2.9 AFM image of MLG transferred from Co foil and placed on SiO <sub>2</sub> /Si substrate. The inset shows step height measurement of MLG. ....	24
Figure 2.10 (a) Device schematic showing bottom electrode (Co foil), MLG and top contact (Ag paste). (b) FESEM image of as grown MLG on Co foil; bottom-left inset shows bare Co foil and top-right inset shows representative Raman spectrum of as grown MLG on Co foil. ....	25

Figure 2.11 Equipment used for CPP MR measurements.....	25
Figure 2.12 Typical CPP MR plots taken from a region that shows predominantly distorted 2D band (as in Figure 2.5 (c) and (d)).....	26
Figure 2.13 Purely CPP negative MR response from the region characterized by the symmetrical 2D band (cases (a) and (b) in Figure 2.5).....	27
Figure 2.14 CPP MR response from the region where ~ 50% of the area shows symmetrical 2D band, whereas the remaining ~ 50% of the area shows distorted 2D Raman band. ....	28
Figure 2.15 Temperature dependence of CPP resistance (R) and magnetic field (B). (a) R vs. T and (b) B (switching field) vs. T of the measured sample (Figure 2.14). ....	28
Figure 2.16 I – V characteristics of the sample in Figure 2.14. (a) at 0 kG and (b) at 11 kG. ....	29
Figure 2.17 (a) Measurements of CPP MR of (Co-grown) MLG transferred on Au electrode at 8 K, 150 K, and 250 K and inset shows optical image of transferred MLG. (b) I-V characteristic of this system at three different temperatures (8 K, 150 K, and 250 K). ....	29
Figure 2.18 CIP-MR of transferred MLG (Co-grown) on glass substrate.....	30
Figure 2.19 CIP I – V characteristics and in-plane R vs. T of MLG transferred on glass. (a) In-plane I – V showing linear and insulating temperature dependence. (b) In-plane resistance showing insulating temperature dependence within the field range of $\pm 11$ kG. ....	31
Figure 3.1 Process flow of fabrication of nanoporous AAO template and growth of MWCNT array.....	35
Figure 3.2 FESEM image of electrochemically deposited Co at the bottom of the nanopores and the inset shows a two-dimensional array of well-regimented nanopores. ....	36
Figure 3.3 FESEM image of as grown CNTs in AAO. Overgrown CNTs covers the top surface.....	37
Figure 3.4 FESEM image of CNTs after removing the overgrowth by ultrasonication. ....	38
Figure 3.5 Schematic diagram of a CNT spin valve device. The CNTs are hosted in an insulating porous alumina template. The barrier layer at Al/Al <sub>2</sub> O <sub>3</sub> interface is partially removed and only a fraction of CNTs are electrically contacted from both sides. The magnetic field is applied along the axis of the tube. ....	38
Figure 3.6 Typical Raman spectra of as-grown MWCNTs. ....	40
Figure 3.7 Spin valve effect observed in Ni-MWCNT-Co spin valve at 8K.....	41

Figure 3.8 Absence of spin valve effect in Ni-MWCNT-Co device at 40K..... 42

# 1 Introduction

## 1.1 Magnetoresistance (MR) Effects in Graphene and Carbon Nanotubes (CNTs)

“Magnetoresistance” (MR) refers to change in electrical resistance of a solid-state system in presence of an externally applied magnetic field [1]. Solid-state devices that exhibit MR effects find application in diverse areas such as data storage and magnetic field sensing [2]. Various types of MR effects exist, which have diverse physical origin. Anisotropic magnetoresistance (AMR) effect has been observed in ferromagnetic granular alloys such as Ni-Fe and Ni-Co [3]. This effect originates from spin-dependent scattering, due to spin-orbit interactions. Giant magnetoresistance (GMR) has been observed in magnetic/nonmagnetic multilayers such as Fe-Cr-Fe layers [4], and Fe/Cr magnetic superlattices [5], which depends on spin-dependent carrier transmission through the multilayers. Tunneling magnetoresistance (TMR) effect has been observed in “magnetic tunnel junctions” (MTJ) in which a thin nonmagnetic tunnel barrier is sandwiched by two ferromagnetic electrodes. Some examples of MTJs are Fe/Al<sub>2</sub>O<sub>3</sub>/Fe [6], and Fe/MgO/Fe [7]. Magnetic field induced metal-insulator transition results in colossal magnetoresistance (CMR) in manganite perovskites that has been observed in La-Ba-MnO [8] and La<sub>0.06</sub>Ca<sub>0.33</sub>MnO<sub>x</sub> [9]. Non-magnetic metals generally exhibit ordinary magnetoresistance (OMR) [10]. This MR originates due to scattering of charge carriers when the magnetic field causes electrons to rotate in circular orbitals with a cyclotron frequency ( $\omega_c$ ). Cyclotron frequency of electrons increases with the magnetic field, which further increases the scattering rate resulting in increased resistance. This OMR effect has been reported in metals such as In, Al, Na, Li, Cu, Ag, Au, etc.

Graphene is a recently discovered two-dimensional material in which carbon atoms are arranged in a honeycomb lattice. Carbon nanotube (CNT) can be viewed as rolled up graphene sheet. Due to their unconventional electronic

structures, graphene and CNT exhibit novel electronic properties and are being heavily investigated as potential channel materials for the next generation of transistors [11]. The unconventional electronic structures of graphene and CNT also lead to novel MR effects [12]–[16]. For example graphene, like zero band gap materials, exhibit linear MR (LMR), which can be explained in both classical and quantum mechanical terms. A classical explanation for LMR is given by Parish and Littlewood [17], where the LMR originates when current direction in a material is deviated from the bias direction by the magnetic field. Quantum linear MR, on the other hand, is generally observed in zero band gap materials with charge carriers of very low effective mass [18], [19]. In these materials, at certain magnetic field a quantum limit occurs where only one Landau level is available for charge transport. The energy gap between the Fermi level and the Landau level increases with increase in magnetic field. The charge injection rate between the Fermi level and the available Landau level decreases with an increasing energy gap that results in linear MR effect. Graphene with its unusual band structure and linear energy dispersion [20], is considered as a perfect platform for the study of LMR [21]. There are many other types of MR effects that are observed in graphene and CNTs [15], [22]–[33]. Some of these effects are described below.

### **1.1.1 Spin-Dependent MR Effects in Graphene and CNT**

Spin-dependent MR is divided in two main categories: (1) MR in spin valve structure in which graphene and CNT are sandwiched between two ferromagnetic electrodes, and (2) small MR effects in modified/doped graphene or CNT which exhibit ferromagnetic property.

In spintronic devices electron's spin degree of freedom is used to control electron transport. Spin valve is a fundamental spintronic device in which a non-magnetic (NM) spacer layer is sandwiched between two ferromagnetic (FM) metals with different coercive fields [34], [35], say  $|H_1|$  and  $|H_2|$  respectively (Figure 1.1). The resistance of the spin-valve can be controlled by an external magnetic field,

and depends on the relative magnetization configuration of the two FM metals. Few examples of spin-valve devices are available in refs. [5], [36], [37].

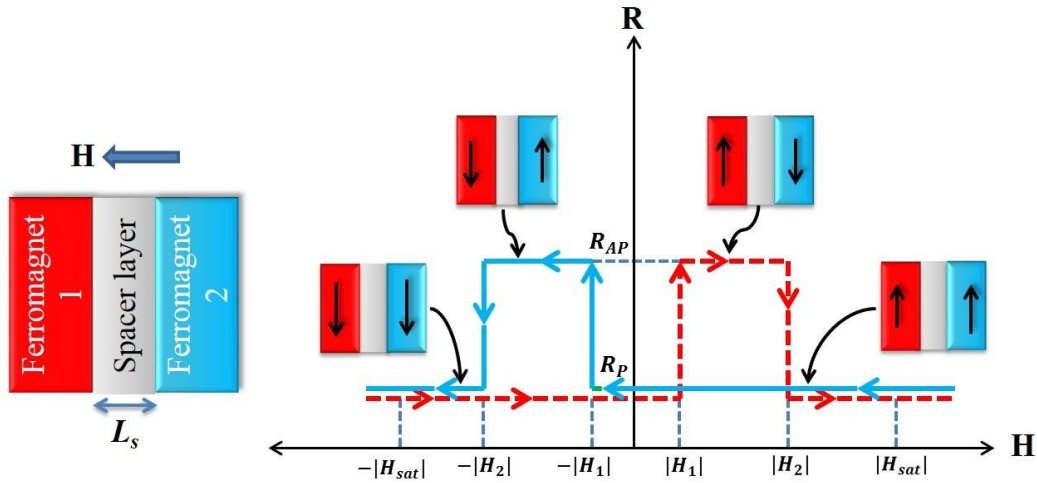


**Figure 1.1** Schematic of a spin valve response.

Ref. [38] reported a graphene spin valve in which single layer graphene (CVD grown on copper foil) is sandwiched between two ferromagnetic (NiFe and Co) electrodes. Tunneling MR of  $\sim 0.4\%$  has been reported at room temperature. In ref. [39], spin-polarized carriers are injected through graphene tunnel barrier within silicon from ferromagnetic electrodes. This indicates that graphene monolayer can be used to avoid the conductivity mismatch problem that prohibits efficient spin injection from metal ferromagnets to semiconductor [40]. In addition, as-grown graphene on a nickel thin film surface has been shown to perform as an oxidation-resistant spin polarizer, which can be integrated with spin valves or magnetic tunnel junctions to achieve superior MR ratios [41].

Multi-walled carbon nanotubes (MWCNTs) are promising material for spin based memory applications since they offer long spin relaxation lengths and time due to very weak spin-orbit and hyperfine interaction [42]–[44]. This translates to well-separated resistance states in MWCNT spin valves, which is desirable for memory devices. Ref. [44] reported a large lateral magnetoresistance effects (61% at 5 K),

in devices where the non-magnetic channel is a multi-wall carbon nanotube bridging epitaxially-grown manganite ( $\text{La}_{0.7}\text{Sr}_{0.3}\text{MnO}_3$ ) electrodes.

Theoretical prediction in ref. [45] reported that hydrogenated graphene nanoribbons can be used in spintronic applications. According to this prediction an adsorbed H atom induces magnetic moments which may interact ferromagnetically or antiferromagnetically depending on the relative adsorption on graphene sublattices. Ref. [46] reported observation of ferromagnetism in H-annealed multi-walled carbon nanotubes (MWCNTs). The reason for inducing ferromagnetism in sufficiently dense disordered MWCNTs is delocalization of pair bonds, which induces excess spin polarization.

### **1.1.2 Spin-Independent MR Effects in Graphene and CNT**

In recent years, magnetoresistance in a single layer graphene as well as graphite has drawn significant attention in the research community [15], [22], [25], [30], [32]. Both CIP and CPP geometries have been studied in detail with various orientations of external magnetic field [15], [22]–[33]. A positive MR is generally reported in highly-oriented pyrolytic graphite (HOPG), with magnetic field perpendicular to the basal plane of HOPG [25]. Metal-insulator transition driven by magnetic field has been observed in CIP and CPP resistivity of graphite, with field parallel to the  $c$ -axis [25], [26]. In refs. [27], [28], the explanation of metal-insulator transition has been provided. This explanation is based on magnetic field-induced breaking of the chiral symmetry and gap-opening in the spectrum of the Coulomb interacting quasiparticles at the corners of the Brillouin zone. This effect is interpreted as the enhancement of the fermion dynamical mass through electron-hole pairing, *i.e.* a transition to an excitonic insulating state [27]–[29], [47]. Metal-insulator transition is absent in the case where the magnetic field is parallel to the plane [29]. On the other hand, multilayer graphene (MLG) generally exhibit a negative MR at low magnetic field range due to weak localization effect [22], [30]–[33]. Due to the reduction of phase coherence time [22], [30]–[33], this negative MR has been found to decrease with increasing

temperature. There are diverse physical origins for a positive MR in MLG sample at higher field range, such as classical and quantum linear MR [15], [22], weak anti-localization [31], [32], and excitonic gap in the Landau level [30].

Since carbon nanotubes come in mainly two forms, large diameter ( $\sim 10 - 30$  nm) multi-walled carbon nanotubes (MWCNTs) and smaller diameter ( $\sim 1 - 2$  nm) single-wall carbon nanotube (SWCNT), they are ideal platforms for studying transport phenomena in low dimensional systems [48]. Extensive investigation of transport mechanism in MWCNTs has been reported in refs. [49]–[53] using magnetoresistance measurements. In ref. [48] negative MR due to one dimensional weak localization (WL) has been reported in a ring of SWCNT. WL originates from constructive interference between conjugate electron waves counter propagating around self-intersecting electron trajectories inside the material [48], [52], [53]. An additional path for interference is acquired by close ring geometry, which results in enhanced backscattering and increased resistance. In presence of magnetic field perpendicular to the SWCNT ring, opposite phases and constructive interference are destroyed in conjugate electron waves [48] resulting in negative MR.

## **1.2 Chemical Vapor Deposition Growth of Graphene and CNT**

Chemical vapor deposition (CVD) is a chemical process in which a carrier gas transports a volatile compound/precursor to a reaction zone where the precursor can either react with other gases or decompose producing non-volatile atomistically thin solid films on a desired substrate and gaseous by-products [54]–[57]. Chemical vapor deposition (CVD) using catalytic metal substrate is the example of fabricating graphene layer through bottom-up approach [58], [59]. CVD has several advantages over mechanical and chemical exfoliation such as large scale and cheap in price for mass production (Figure 1.2). CVD is widely used in coating, fabrication of bio, transparent conducting layers, electronics, and photonics [11]. One of the simplest methods for the synthesis of CNTs is thermal Chemical Vapor Deposition (CVD). In this method, silicon substrate deposited

with metallic catalysts (for example Fe, Ni) is used as the base material on which CNTs are grown. The growth process is based on the decomposition of carbon precursor at high temperatures (6000–1000 °C). This CVD approach allows patterning of catalyst and hence CNTs can be grown at desired location for device applications. There are two types of growth models for CNTs depending on the location of the catalyst particles after growth. The tip growth model refers to cases when the catalyst stays at the tip of the CNTs. The base growth model applies to cases when the catalyst stayed at the base of the CNTs [60]–[63].

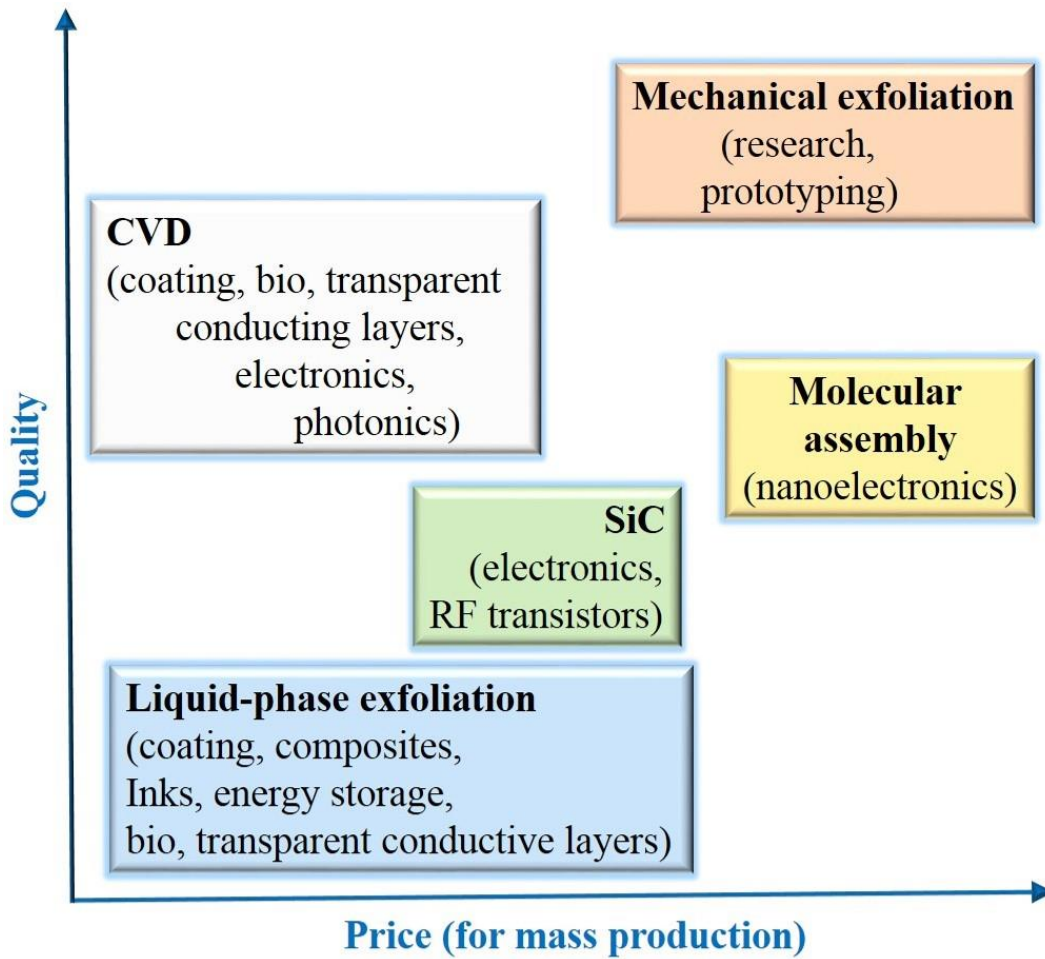


**Figure 1.2** Different methods of producing large-scale graphene. CVD allows growth of high quality graphene at a low cost (adapted from ref. [11]).

In this thesis, a CVD technique has been used to grow multilayer graphene and multi-wall carbon nanotubes on ferromagnetic metal catalyst.

### 1.3 Raman Spectroscopy of Carbon Nanotubes and Graphene

Raman spectroscopy [64] is a versatile and non-destructive characterization tool for studying the structural and electronic properties of carbon nanotubes and graphene. Elastic light scattering (Rayleigh) spectroscopy [65], [66] has been used to count the number of layers of graphene in a sample, but this method is limited to exfoliated graphene on optimized substrate and does not provide any structural and electronic property. Raman spectroscopy, on the other hand, is able to identify defects and structural changes that occur during processing or transfer steps. Raman spectroscopy is invaluable for quality control of samples during entire process flow, starting from growth to measurement of final device [67].

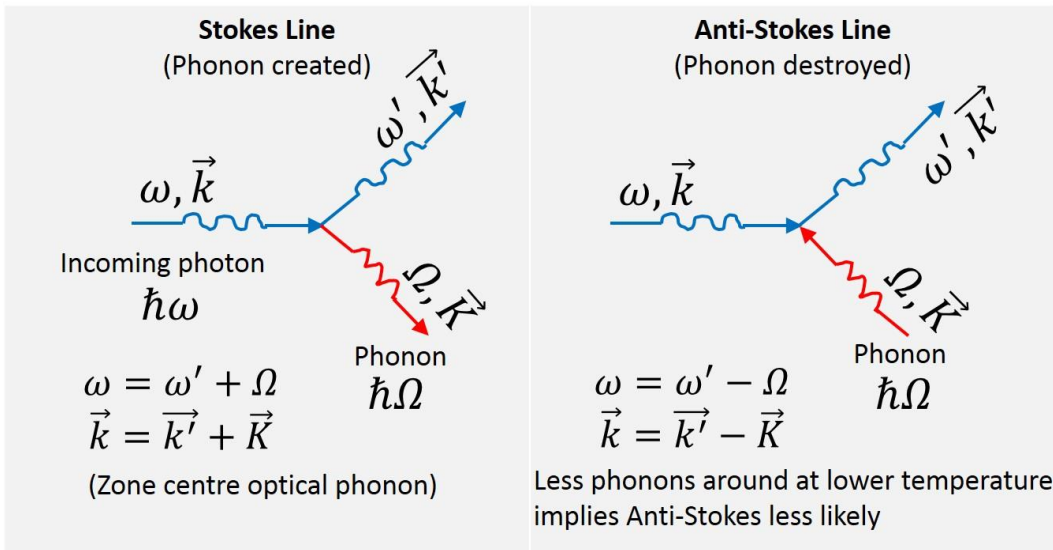


**Figure 1.3** Raman scattering process (not drawn to scale), left panel showing Stokes process and the right panel is Anti-Stokes process (adapted from ref. [68]).

Raman scattering is the inelastic scattering of photons by optical phonons (mainly  $K \cong 0$  phonon), whereas Brillouin scattering is the inelastic scattering of photons by acoustic phonons. Rayleigh scattering takes place when the system returns to its initial state, and the frequency of an emitted photon remains the same as the initial one (also called elastic scattering).

Raman scattering happens when, a photon strikes the sample and loses part of its energy in the interaction process, resulting in lower energy after coming out of the

sample. This corresponds to Stokes line (process). On the other hand, if the incoming photon strikes on the sample, which is already in the excited vibrational state, the photon can leave the crystal with an increased energy. This process is known as anti-Stokes. Given that Stokes is most probable [68], [69], almost every Raman spectra in literature of carbon nanotube and graphene, report Stokes line intensity measurement as function of Raman shift (difference between incident and scattered photon energy) [70]. The complete process involved in inelastic scattering of photons by phonons is shown in Figure 1.3.

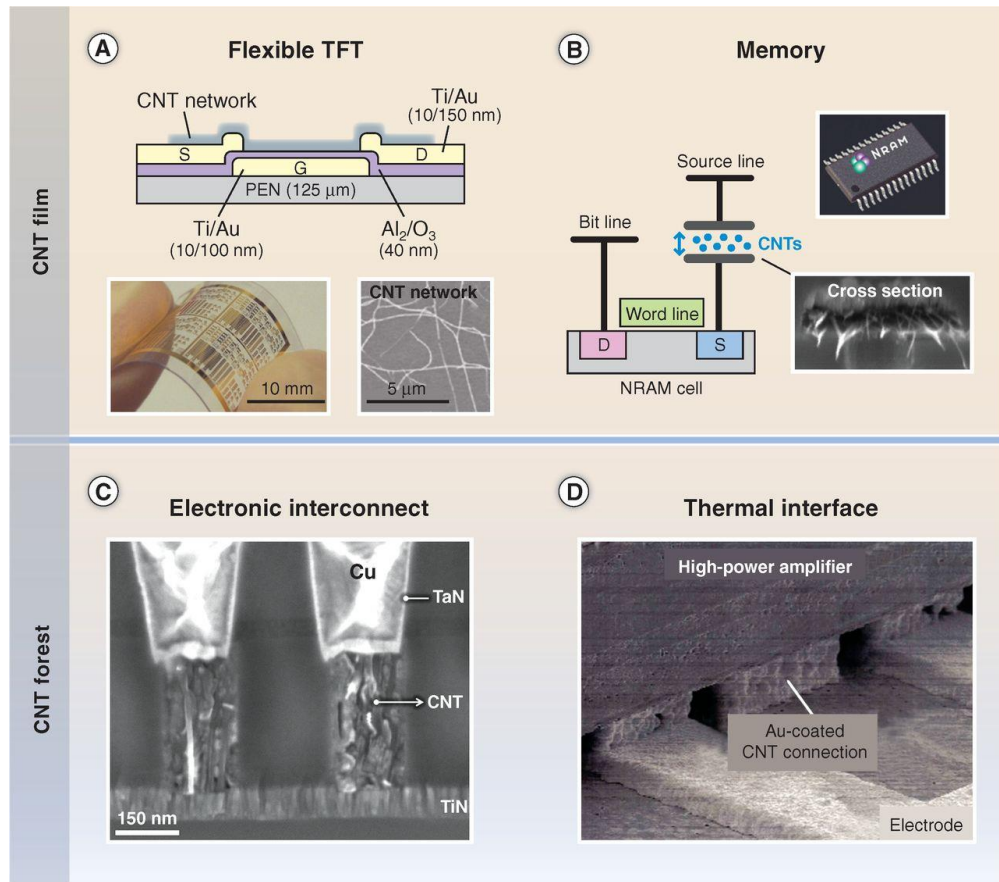


**Figure 1.4** CNT applications in microelectronics. (A) Flexible TFTs using CNT networks deposited by aerosol CVD. (B) CNT-based nonvolatile random access memory (NRAM) cell (C) CMOS-compatible 150-nm vertical interconnects (D) CNT bumps used for enhanced thermal dissipation in high power amplifiers. (taken from reference [71]).

## 1.4 Motivation of This Work

There are many potential applications that could make use of carbon nanotubes and graphene. For example, as shown in Figure 1.4, carbon nanotubes can be used in flexible thin-film transistors [72], memories [73], electronic interconnects [74], and thermal interfaces [75], whereas graphene can be used in spintronics [76], [77], photonics [78], [79], nanoelectronics [80], transparent conducting layers in flexible electronics [81], sensors [82], and bio-applications [83]. Significant research is on-going with the aim to explore all of these possibilities. This thesis focuses on magnetoresistance (MR) effects in graphene and carbon nanotubes.

Current-perpendicular-to-plane (CPP) magnetoresistance effect is extensively used in state-of-the-art magnetic field sensing and data storage devices [84]. The existence of CPP-MR in these systems depend on spin-dependent carrier transmission through magnetic/non-magnetic multilayer. In this work, we have explored an alternative layered system in which multilayer graphene is grown on cobalt foil. These systems also give rise to large CPP MR effects, which have not been reported in literature. Unlike conventional MR effects, our observed MR does not depend on spin-polarized carrier transmission. Due to the polycrystalline nature of cobalt foil, we have observed non-uniformity in graphene growth on the surface. Depending on nature of cobalt-graphene interaction and as well as interlayer coupling between graphene layers away from the interface, one can observe different MR ratios and sign (positive and negative).

The unusual conducting properties of carbon nanotubes offer intriguing possibility for spin electronic devices. In fact it has been found that spin relaxation length of carbon nanotubes is extremely long [50], [85], which can be attributed to weak spin-orbit and hyperfine couplings in these systems. Thus vertical array of carbon nanotubes may be utilized to create a high-density array of magnetic random access memory (MRAM) cells. Most of the previous studies on carbon nanotube spin valves report only single CNT (either single-wall or multi-wall) in lateral geometry [42]–[44]. However, for magnetic random access

memories, high-density integration of carbon nanotube spin valves and their room temperature operation are required. In the past, single MWCNT spin valve has been demonstrated in ref. [42], where a maximum change in resistance was 9% with estimated spin relaxation length of 130 nm. Ref. [43] reports a remarkable increase of the MR ratio with decreasing junction bias, reaching a maximum MR ratio of 30% at a junction bias current of 1 nA in MWCNT contacted via Co. Ref. [44] reported a large magnetoresistance effects (61% at 5 K), in devices where the non-magnetic channel is a multiwall carbon nanotube that spans a 1.5  $\mu\text{m}$  gap between epitaxially-grown and highly spin-polarized [86], [87] manganite ( $\text{La}_{0.7}\text{Sr}_{0.3}\text{MnO}_3$ ) electrodes. All these previous experiments indicate the possibility of realizing well-separated resistance states in MWCNT spin valve, which is a key prerequisite for memory devices. Even though single MWCNT spin valves have been demonstrated [42]–[44], high density integration of such memory elements are largely underdeveloped [88]–[90]. In this work, we present one possible method to fabricate the spin valve memory cells in the highly ordered hexagonal nanoporous anodic alumina oxide (AAO) template. Previous result with similar method has shown poor spin valve response [88] due to long channel length and/or poor MWCNT quality. In this work, we report short channel length MWCNT (embedded in AAO) spin valve.

## **1.5 Work Completed to Date**

Two main projects have been completed. First, current-perpendicular-to-plane magnetotransport measurements in as-grown multilayer graphene on cobalt foil using chemical vapor deposition, and second, fabrication and characterization of vertical array of carbon nanotube spin valves.

### **1.5.1 Magnetoresistance Effects in As-Grown MLG on Co Foil**

In this study large-area multilayer graphene (MLG) samples (with a typical dimension of 2 cm  $\times$  2 cm) as-grown on cobalt (Co) foil using chemical vapor deposition (CVD) technique have been used. Magnetoresistance (MR) effect has been reported in current-perpendicular-to-plane (CPP) and current-in-plane (CIP)

geometries. It has been shown that both positive and negative MR manifest in CPP geometry. Details of this work have been described in Chapter 2 of this thesis.

### **1.5.2 Spin Valve Effect in High Density Array of Multi-Walled Carbon Nanotubes**

In this study high-density array of multi-wall carbon nanotubes (MWCNTs) was fabricated in nanoporous anodic alumina oxide (AAO) template. The CVD growth technique was employed, which results in ~ 60–70 nm of tube diameter and 700 nm of tube length. Magnetoresistance measurements on these structures reveal spin valve effect at low temperature. Details of this work have been reported in Chapter 3 of this thesis.

## **1.6 Future Work**

A potential future project related to Chapter 2, is to explore spin filtering capability of hybridized interface of as-grown MLG on catalytic surfaces (such as Co, Ni and/or h-BN). A theoretical prediction of this effect has been made in ref. [91], however no experimental work has been reported to date. An ideal spin filter would allow all carriers with one spin to pass through but none with the other spin [92]. Such perfect spin filtering may be achievable by controlling the thickness of graphene layer, improving quality, uniformity, and realizing better contact with MLG.

To get a stronger spin valve signal in our vertical Co/MWCNTs/Ni spin valves reported in Chapter 3, the following modifications can be tried. For example, improving MWCNT quality, improving ferromagnet-MWCNT contact, and reducing scattering by using single-wall carbon nanotube instead of MWCNTs can potentially improve the quality of spin valve signal. Further details are provided in Chapter 4 of this thesis.

## 2 Experimental Study of c-axis MR in Multilayer Graphene as-Grown on Co Foil

### 2.1 Introduction

The past decade has witnessed emergence of various two-dimensional atomic crystals such as single layers of graphite (or, “graphene”), boron nitride, dichalcogenides [93], and rapid progress in their fabrication and exploration of device properties [94], [95]. A vast majority of this work has been targeted at graphene, a single graphitic sheet in which  $sp^2$ -hybridized carbon atoms are arranged in an atomically thick two-dimensional honeycomb lattice [96]. Graphene fabrication can be realized both via top-down and bottom-up approaches [11], [97]. The standard method uses a *top-down* approach such as mechanical and chemical exfoliation. During the initial stage of this development graphene was fabricated using mechanical exfoliation from highly oriented pyrolytic graphite (HOPG) [93], [95]. Mechanical exfoliation is the process by which mechanical force is used to separate graphene layer from the bulk graphite. This is most popular way to fabricate graphene because of easy production and low cost. Few examples of exfoliation are, (a) micromechanical exfoliation (few layer graphene films with lateral sizes up to 10  $\mu\text{m}$  and thicknesses of less than 10 nm) [93], [98], (b) ultrasound treatment in solution (liquid-phase exfoliation) [99], (c) solution based intercalation steps [100], and (d) liquid medium exfoliation of graphite using wet ball milling [101]. There are still some challenges, in spite of great success achieved in exfoliation process. Particularly, in chemical exfoliation, we need to overcome the strong van der Waals forces that stick graphene sheets together. The interlayer cohesive energy or exfoliation energy for graphite is defined as the energy per unit area required to overcome the van der Waals forces when peeling two sheets apart [99], [102]. Theoretical calculation suggests that we need the energy of 2 eV/nm<sup>2</sup> to separate the graphene layer from graphite [102]. Polar solvent N-Methyle-2-pyrrolidone (NMP) has

been found to be more suitable for exfoliating graphite into monolayer graphene sheets [99]. The main issue of this process is that it does not provide sufficient output yield, purity, and gives defective graphene (such as atomic defects, wrinkles or ripples) and strain in it [103]. This method has limited scalability and generally produces a small area ( $\sim$  tens of microns) graphene. For both mechanical and chemical exfoliation, mainly three types of graphite have been used, *natural flake* (poor crystallinity in terms of rotational stacking faults and impurities but can be exfoliate faster), *kish* (obtained from byproduct of steel making process, contains iron impurities) and *synthetic* (highly ordered pyrolytic graphite, known as HOPG, with excellent Bernal stacking of the graphene layers with less than  $1^\circ$  rotational mismatch and very low impurity content).

*Bottom-up* approach of graphene synthesis includes chemical vapor deposition (CVD) on catalytic metal substrates (Ni, Cu) and growth on SiC [11], [58], [59], [97], [104], [105]. CVD has several advantages over top-down fabrication methods (discussed above) in terms of large area, and lower price for mass production. Graphene grown by CVD needs to be removed from the underlying substrate for subsequent device synthesis [95], [104], [105]. Also CVD-grown graphene generally exhibits lower in-plane mobility compared to mechanically exfoliated graphene due to presence of grain boundaries and associated carrier scattering.

Apart from the unique properties offered by pristine graphene, as-grown graphene on catalytic ferromagnet metals have attracted significant attention of late due to possibility of observing novel spintronic effects such as “perfect spin filtering” [92] and “giant Rashba splitting” [106]. Depending on the nature of the catalytic substrates, graphene can form either a physisorption interface or a chemisorption interface [107]–[110]. Physisorption interface is generally formed when graphene is CVD grown on Cu. Such interface is characterized by weak interfacial bonds and the interfacial graphene layer preserves its pristine electronic structure with possible shifting of the Fermi level from the Dirac point depending on the nature

of interfacial charge transfer. Cu-grown samples typically exhibit fewer number of graphene layers due to the low solubility of carbon in copper. These samples also exhibit grain boundaries, which results in a defect (“*D*”) peak in the Raman spectrum. Chemisorption interfaces, on the other hand are formed when graphene is CVD grown on ferromagnetic (such as Ni, Co) substrates. In this case the out of plane  $3d$  orbitals of the ferromagnets strongly overlap with the out of plane  $p_z$  orbital of the carbon atoms and form a chemical bond. As a result the interfacial graphene layer adopts an electronic structure that is significantly different than pristine graphene. Such changes include elimination of the Dirac point, band opening and possible introduction of defect states in the band gap. As a result, a defect peak is observed in the corresponding Raman spectrum. The subsequent graphene layers however resemble pristine graphene. The presence of ferromagnetic catalyst also affects the interlayer coupling between the graphene layers as evidenced by the symmetry of the  $2D$  peak in the Raman spectrum under certain growth conditions. For thicker graphitic films, the layers away from the interface, exhibit no defect (*D*) peak.

As mentioned before, multilayer graphene (MLG) CVD-grown on ferromagnetic substrates can potentially operate as a “perfect spin filter” [92] and if realized can enhance the performance of myriad spin-based memory and information processing devices. A giant Rashba splitting has also been observed in Ni-graphene interfaces, with implications in spin-based classical and quantum information processing [106]. Motivated by these initial studies, a series of magnetoresistance (MR) measurements have been performed in the current-perpendicular-to-plane (CPP) configuration on ferromagnet-graphene stacks [38], [39], [41], [91], [106], [111], [112]. However all of these studies relied on “transferred” graphene, i.e. graphene layer was physically transferred on the ferromagnetic substrate [38], [39]. In such configurations, however, the chemisorption interface does not form and only small MR ratios have been

reported so far. The transfer steps also affect the interlayer coupling as observed from the Raman spectra of the transferred specimens.

Our previous work focused on CPP-MR of as-grown MLG on Ni [47]. We reported a very large negative CPP MR effect, which is weakly dependent on temperature and even persists at room temperature [47]. This effect originates from interlayer tunneling of charge carriers between weakly coupled graphene layers. To explore if such features are common to MLGs grown on other ferromagnetic substrates as well, here we explore CPP MR effect of MLG as-grown on cobalt substrates via CVD. We find that large MR effects manifest in such MLG-ferromagnet junctions and persist at room temperature. Such effects have not been reported before in other graphene-based systems.

For growth of MLG, Co foils have been chosen as the substrate. A number of experimental studies have been reported in literature, which investigated the growth of graphene on (a) polycrystalline cobalt (Co) thin films deposited on SiO<sub>2</sub>/Si [113]–[116] and (b) single crystal Co films on c-plane (0001) sapphire (Al<sub>2</sub>O<sub>3</sub>) [117]. In case of polycrystalline thin films of Co, mixture of monolayer to multilayer graphene (MLG) have been detected using various technique such as Raman spectroscopy, optical microscopy, FESEM, and TEM [118]. But, on the other hand for single crystal Co film on sapphire substrate showed monolayer behaviour [119]. Metal-catalyzed (Co or Ni thin films of 100–300 nm) crystallization of amorphous carbon (a-C) have shown layers of graphene depending on film thickness [120]. Ref. [118] reported graphene growth on Co foil via flame synthesis, using methane as a fuel. Carbon atoms readily dissolve within the Co substrate (given higher solubility compared to Cu), with graphene growth ensuing upon cooling.

## 2.2 Experimental Methods

### 2.2.1 Growth of MLG on Cobalt (Co) Foil

In this work, Co foil (0.025 mm, 99.95% metal basis) [CAS # 7440-48-4, Stock # 40183, and Lot # H25X052] purchased from Alfa Aesar has been used as catalytic metal substrate for growth of MLG. Commercial Tystar low-pressure chemical vapor deposition (LPCVD) chamber is used to grow MLG on Co foil. The typical surface images of the Co foil, before and after MLG growth, are shown in Figure 2.1. The polycrystalline nature of the Co foil is evident from the X-ray diffraction spectrum as shown in Figure 2.2.

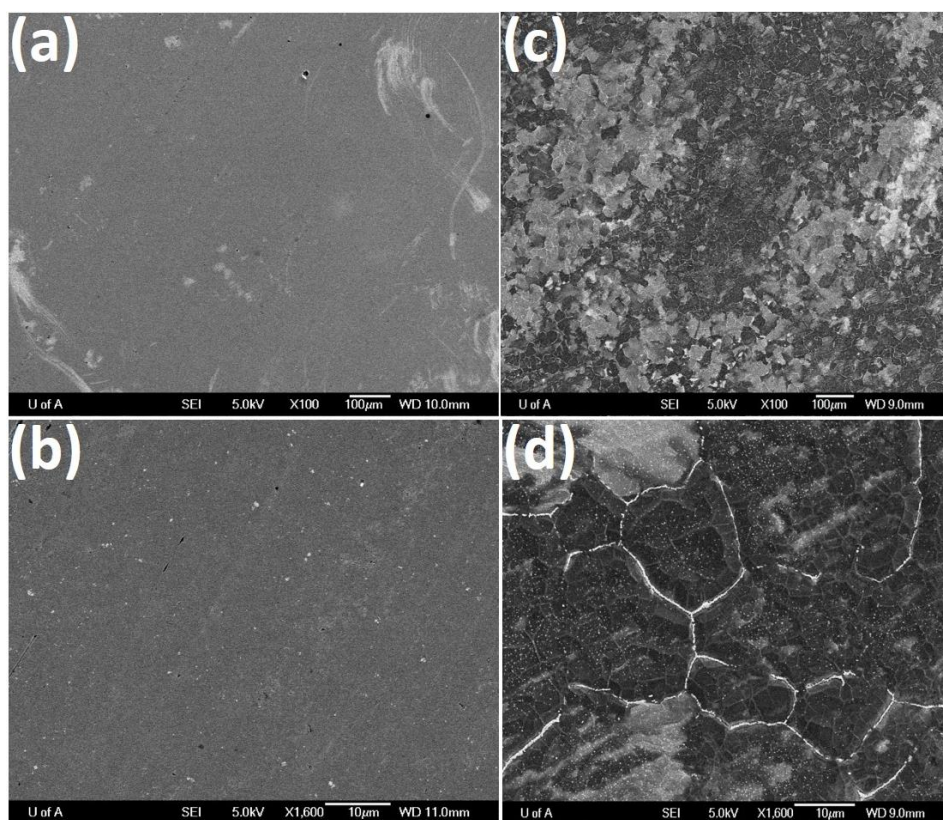


**Figure 2.1** Field emission scanning electron microscope (FESEM) image of (a), (b) bare Cobalt (Co) foil and (c), (d) as grown multilayer (MLG) graphene on Co foil at different magnifications.

According to ref. [117] the peak at  $\sim 44^\circ$  in the XRD spectrum represents Co hcp (0002) or Co fcc (111) phase. The LPCVD process flow consists of the following

steps: (a) Co foil ( $\sim 1.5 \text{ cm} \times 1.5 \text{ cm}$ ) load, (b) furnace purge, (c) temperature ramp to  $1000 \text{ }^\circ\text{C}$  and hydrogen anneal for one hour, (d) graphene growth at  $1000 \text{ }^\circ\text{C}$  for 10 minutes, (e) natural cooling, and finally (f) unloading of the sample. We have used  $0.3\% \text{ CH}_4$ ,  $9.7\% \text{ H}_2$ , and  $90\% \text{ Ar}$  during the growth of graphene. The extensive hydrogen-annealing step mentioned above eliminates the presence of any native oxide on the cobalt surface and improves grain size. Due to polycrystalline nature of catalytic Co foil (as confirmed via XRD spectrum, Figure 2.2), as-grown MLG has different thicknesses at different regions of the Co surface. Representative Raman characterization confirming this feature is reported in the next subsection. Higher concentration of carbon-containing species within the chamber leads to bulk graphite growth on the Co surface.

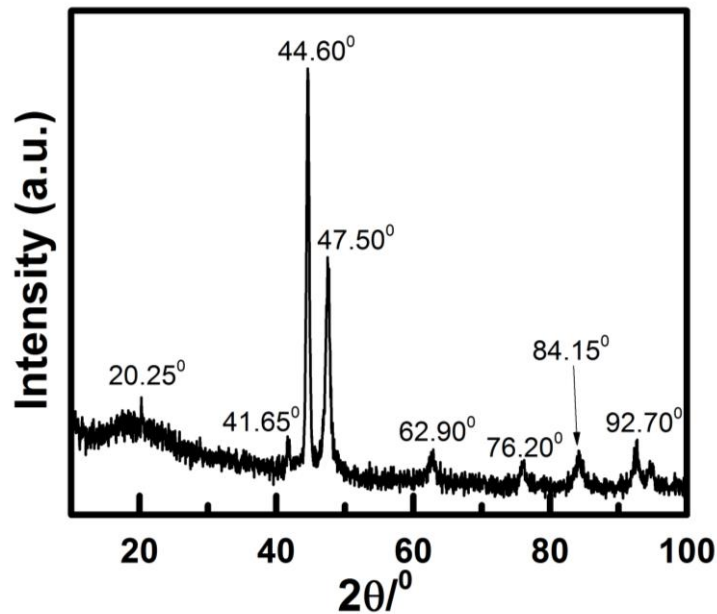


**Figure 2.2** XRD spectrum of as-purchased Co foil (from Alfa Aesar). Presence of several peaks indicates the polycrystalline nature of the Co foil.

### 2.2.2 Device Fabrication: Process Flow

In the synthesis process described above, graphene growth occurs on both sides of the Co surface since the bottom surface is also accessible by the carbon containing species in the LPCVD chamber.

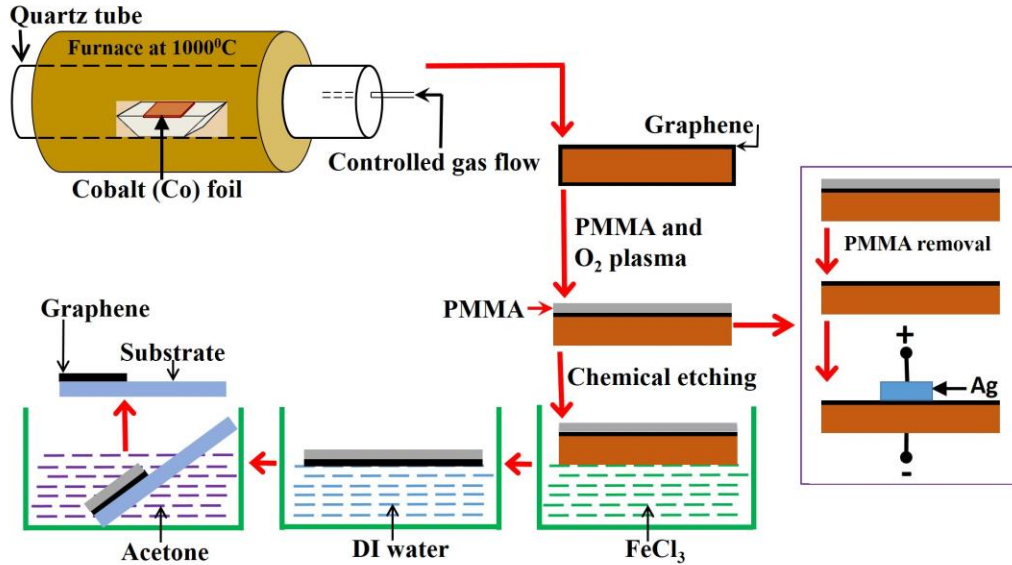


**Figure 2.3** Schematic diagram of MLG growth and transfer on arbitrary substrate.

Therefore to fabricate the final device, we selectively remove graphene from the bottom surface to expose the Co substrate. This Co substrate acts as the bottom electrical contact for CPP measurements. To achieve this we coat PMMA (polymethyl methacrylate purchased from Micro Chem) protective layer on the top MLG surface and let it dry for ~ 12 hours. The bottom surface of the sample, which is not coated with PMMA, is directly exposed to O<sub>2</sub> plasma in Tegal 901e Plasma Etcher and MLG is etched away using descum recipe. After complete removal of graphene from the bottom surface, we remove the PMMA from the top surface using acetone. Finally electrical contacts are made by silver epoxy. The complete process flow of MLG growth and transfer is shown in Figure 2.3. Optical image of O<sub>2</sub> plasma etched sample is shown in Figure 2.4.

For the reference samples, MLG has been transferred to another electrode (generally Au) using the following procedure (Figure 2.3). First, MLG is removed from bottom surface using the same oxygen plasma etching procedure described above. Next, we remove the Co substrate using FeCl<sub>3</sub> etchant for 6 hours at 50 °C.

After complete etching of Co, PMMA supported MLG floats up in the etchant solution.

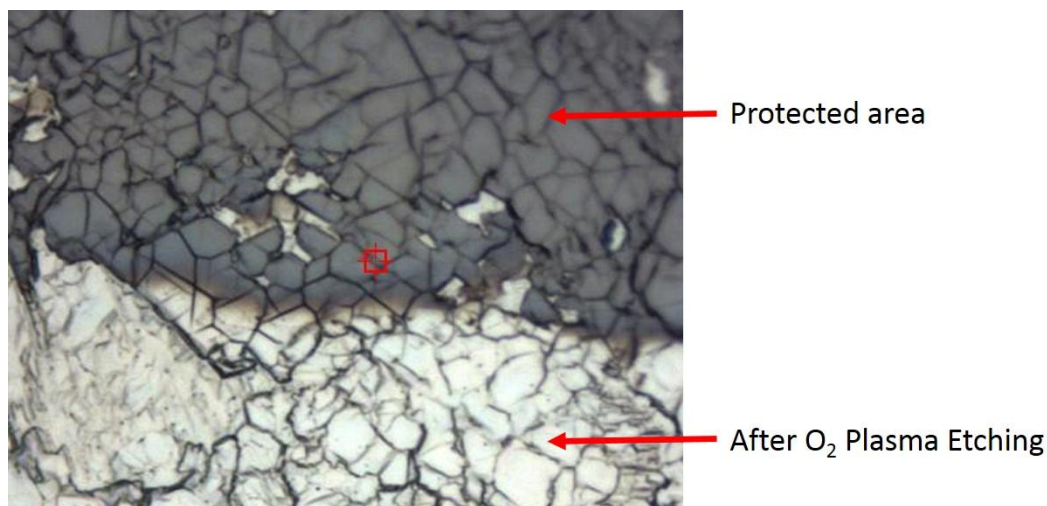


**Figure 2.4** Optical image of as-grown MLG on Co foil. Top half of the sample is protected and the bottom half is exposed to O<sub>2</sub> plasma etching.

PMMA supported MLG is carefully transported into deionized water for cleaning purpose and then transferred to Au electrode (fabricated on SiO<sub>2</sub>/Si). The sample is kept in desiccator for ~ 12 hours for complete drying including removal of any water/air trapped in between graphene and Au electrode. This sample is then heated at 50 °C for 30 minutes for complete adhesion of graphene and electrode, which will enable reliable electrical measurements in the CPP geometry. Finally, top PMMA is removed using acetone. An image of transferred graphene on Au electrode is shown in inset of Figure 2.17 (a).

### 2.2.3 Raman Spectroscopy of MLG As-Grown on Co

Raman spectroscopy has been used to extensively characterize the as-grown and transferred MLG. Representative Raman spectra of the as-grown MLG/Co samples are shown in Figure 2.5. All Raman measurements have been acquired at room temperature using a Nicolet Almega XR micro-Raman Analysis System. Laser wavelength has been set to 532 nm (2.33 eV). Maximum power has been set to 24 mW, 100% of which has been used for this spectroscopic study. All

Raman spectra were collected by fine-focusing a  $50\times$  microscope objective. Four distinct regions (Figure 2.5) on the sample have been identified from this Raman study: (a) intensity of the 2D peak ( $I_{2D}$ , occurring at  $\sim 2693\text{ cm}^{-1}$ ) is stronger than the intensity of the G peak ( $I_G$ , occurring at  $\sim 1580\text{ cm}^{-1}$ ) and the 2D peak is symmetric and can be fitted by a single Lorentzian, (b)  $I_{2D} < I_G$  but the 2D peak (now occurring at  $\sim 2698\text{ cm}^{-1}$ ) can still be fitted by a single Lorentzian, (c)  $I_{2D} < I_G$  and the 2D peak ( $\sim 2715\text{ cm}^{-1}$ ) shows a “shoulder” on the lower frequency side

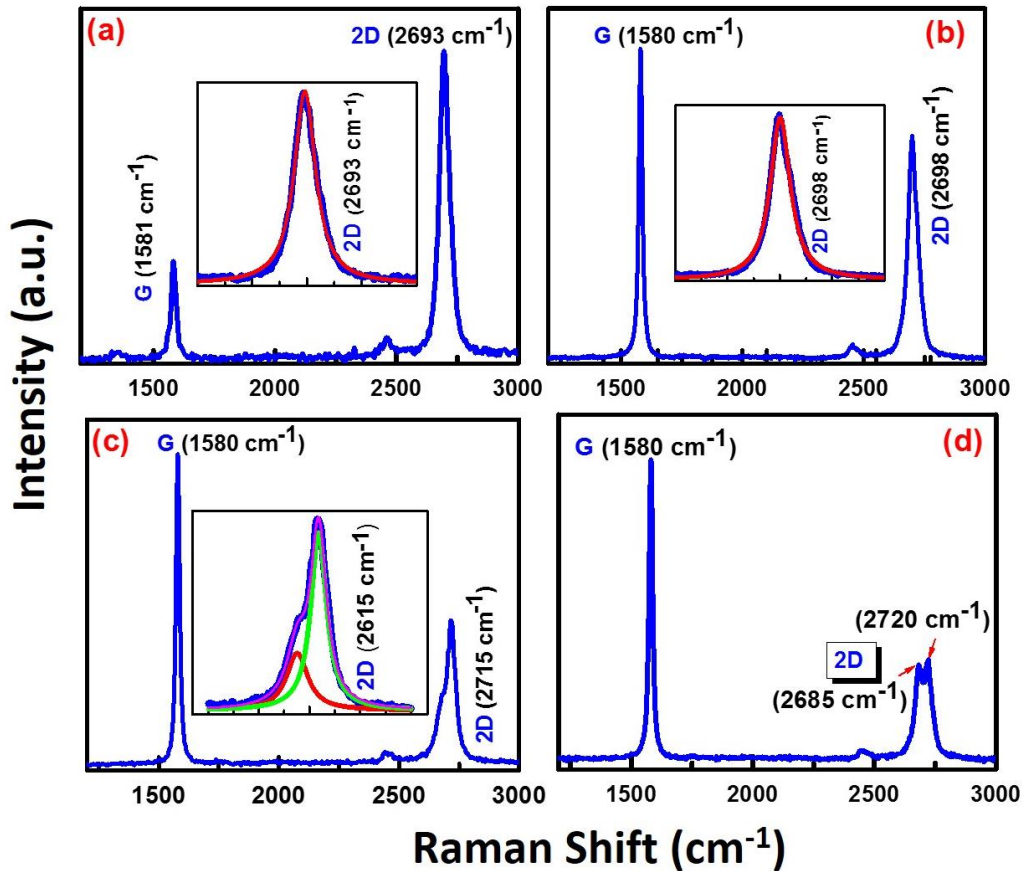


**Figure 2.5** Representative Raman spectra of as-grown MLG on Co foil (a)  $I_{2D} > I_G$  and 2D peak is symmetrical (b)  $I_{2D} < I_G$  and 2D is still symmetrical (c)  $I_{2D} < I_G$  and 2D shows HOPG-like shoulder (d)  $I_{2D} < I_G$  and 2D peak ( $\sim 2685\text{ cm}^{-1} - 2720\text{ cm}^{-1}$ ) is split into sub-peaks.

of the 2D band and cannot be fitted by a single Lorentzian and (d)  $I_{2D} < I_G$  and the 2D peak ( $\sim 2685 - 2720\text{ cm}^{-1}$ ) is split into sub-peaks and cannot be fitted by a

single Lorentzian. In case (c), the Raman spectrum is reminiscent of that observed in highly oriented pyrolytic graphite (HOPG). In all of the above cases a strong  $G$  peak is present at  $\sim 1580 \text{ cm}^{-1}$ , which attests to presence of hexagonal graphene lattice. Further, there is no defect ( $D$ ) peak (at  $\sim 1350 \text{ cm}^{-1}$ ) in any region of our samples indicating absence of defect states due to missing carbon atoms or impurities at grain boundaries. For the purpose of comparison, Raman spectrum of bulk graphite (HOPG- SPI-1 grade,  $10 \times 10 \times 1 \text{ mm}^3$  in size, from SPI supplies) is shown in the Figure 2.6 (b). The two characteristic peaks occur at  $\sim 1580 \text{ cm}^{-1}$  and  $\sim 2718 \text{ cm}^{-1}$  which are commonly labeled as  $G$  and  $2D$  band respectively [104], [121], [122]. The  $2D$  peak for HOPG is asymmetric as shown in the inset of the Figure 2.6 (b) and has a shoulder on the left side of the main peak [123].

In the regions where  $I_{2D} > I_G$  (corresponding to (a) mentioned above), the ratio  $I_{2D}/I_G \sim 2 - 3$  and the full width at half maximum (FWHM) of the  $2D$  peak is  $\sim 47 \text{ cm}^{-1}$ . These values indicate the presence of multiple graphene layers (MLG) on the Co surface since monolayer graphene generally gives rise to slightly stronger  $I_{2D}/I_G$  ( $\sim 4$ ), narrower  $2D$  FWHM of  $\sim 30 \text{ cm}^{-1}$  and  $2D$  peak location at lower frequency of  $\sim 2675 \text{ cm}^{-1}$ .

To evaluate the number of layers we have performed atomic force microscopic studies and step height measurements after transferring the MLG on  $\text{SiO}_2/\text{Si}$ . Interestingly, a thickness of  $\sim 25 \text{ nm}$  has been obtained (in the area characterized by Figure 2.5 (a)) which indicates  $\sim 50$  layers of graphene as shown in Figure 2.9. In spite of this large thickness, the  $2D$  peak is symmetric (in the regions corresponding to Figure 2.5 (a)) and therefore indicates weak interlayer coupling between the individual graphene layers in these regions. We note that the presence of interlayer coupling introduces splitting and other forms of asymmetry in the  $2D$  band (as in (c), (d)). Thus in the regions corresponding to (a), the MLG essentially represents turbostratic graphite [104], [124]–[127], in which individual graphene layers are weakly coupled to each other. A similar conclusion can be

drawn for region (b), which has slightly larger number of layers (as evidenced by  $I_{2D} < I_G$  and  $2D$  FWHM of  $\sim 44$   $\text{cm}^{-1}$ ) but nevertheless the  $2D$  peak can still be fitted by a single Lorentzian and hence the layers appear to be weakly coupled.

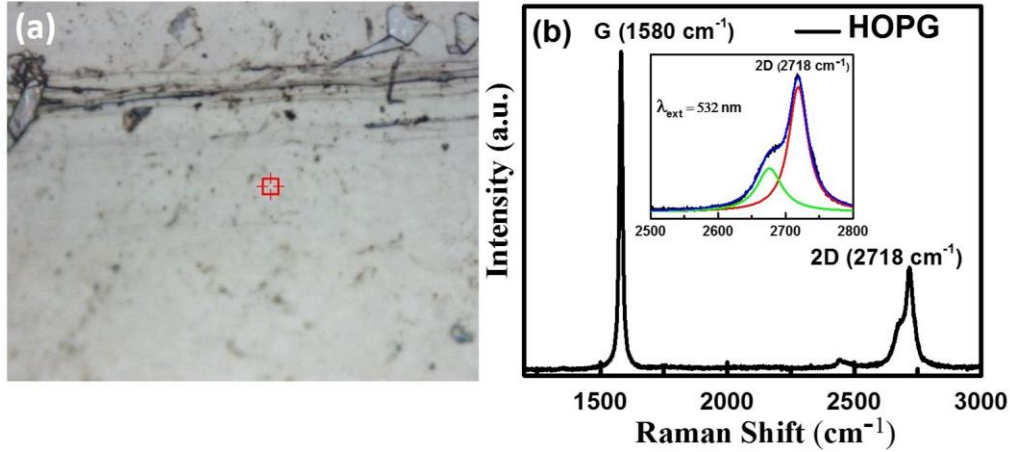


**Figure 2.6** (a) Optical image of highly oriented pyrolytic graphite (HOPG as acquired from SPI supplies). (b) Raman spectrum of HOPG. The inset shows the  $2D$  band which can be fit by two Lorentzians.

In the remaining regions (characterized by (c) and (d) mentioned above)  $I_{2D} < I_G$  and the  $2D$  peak is distorted and cannot be fitted by a single Lorentzian. In these regions the interlayer coupling is stronger, which causes the distortion in the  $2D$  band.

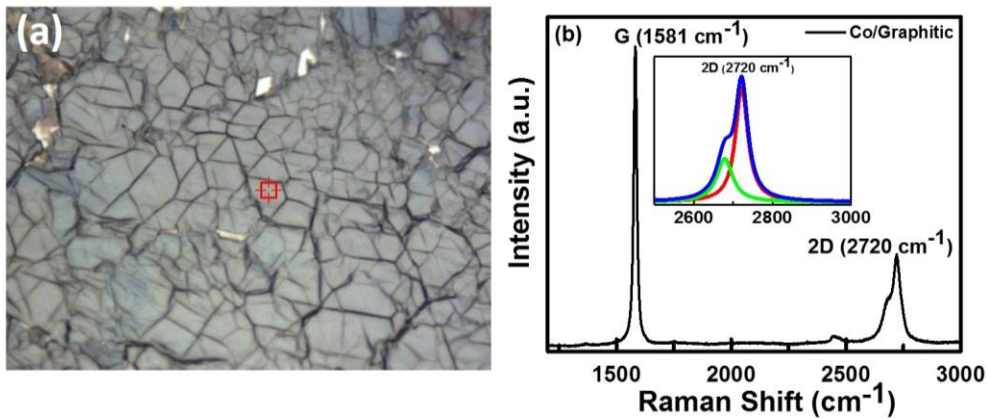


**Figure 2.7** (a) Optical image of MLG/Co surface (b) HOPG like Raman spectrum of MLG/Co sample, inset showing  $2D$  band with two Lorentzian fitting.

The variation in interlayer coupling is presumably related to the polycrystalline nature of the Co substrate as evidenced by Figure 2.2. The presence of multiple graphene layers is consistent with previous studies that reported higher number of layers for substrates with larger thickness [128].

#### 2.2.4 MLG/Co Surface Morphology and Step Height Measurement Using Atomic Force Microscopy (AFM)

We used AFM (Asylum Research, MFP-3D) under ambient conditions with a standard tetrahedral silicon tip (Olympus, OMCLAC160TS-W2) located at the end of a silicon cantilever to determine the surface roughness profile of CVD-grown MLG-on-Co (Figure 2.8). Under AC mode, the typical values of force constant, resonant frequency and scan rate were 42 N/m, 300 kHz and 1 Hz respectively. The radius of curvature of the tip is  $< 10$  nm.

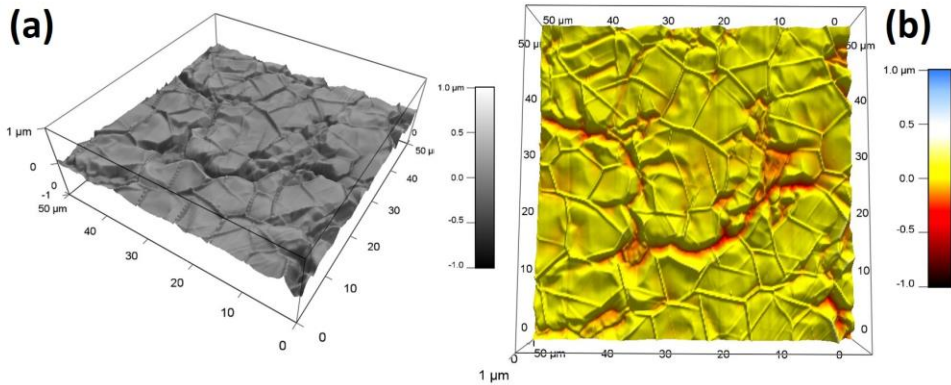


**Figure 2.8** 3D Atomic force microscopy (AFM) surface morphology of as-grown epitaxial MLG on Co foil.

Minimum step height of the transferred MLG on  $\text{SiO}_2/\text{Si}$  substrate was  $\sim 20$  to  $30$  nm (Figure 2.9). In case of MLG-on-Ni, fcc and hcp domains of the graphene are possible, depending on the adsorption geometry of the carbon atoms on Ni (111) surface [47], [129]. According to this work, the grain boundaries are often “delaminated” from the Ni substrate and bulge away from the Ni substrate. These features allow matching of fcc and hcp domains by a continuous sheet of graphene, without formation of defects. In our MLG-on-Co samples we have

observed similar bulging features as shown in Figure 2.8. This is presumably the reason for not observing  $D$  peak in the grain boundaries of our MLG-on-Co samples.

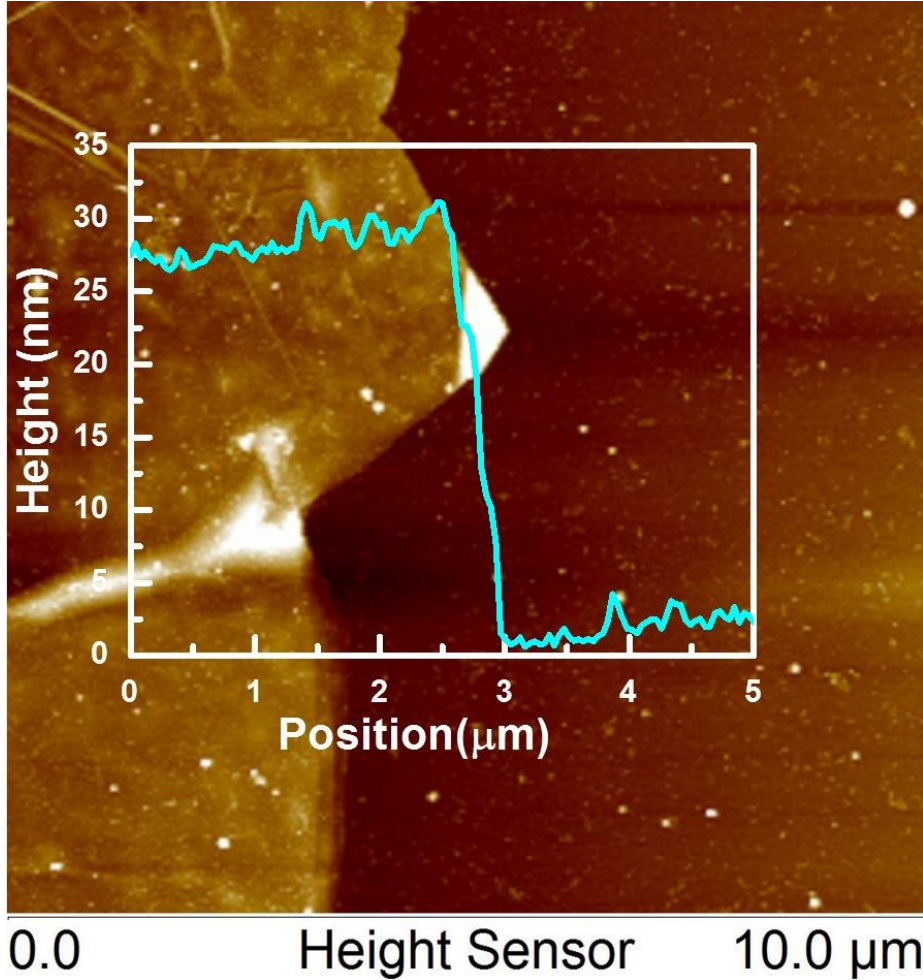


**Figure 2.9** AFM image of MLG transferred from Co foil and placed on SiO<sub>2</sub>/Si substrate. The inset shows step height measurement of MLG.

### 2.2.5 Device Structure

For CPP MR measurement, top contact is made on graphene and bottom contact is made on Co using silver epoxy ( $\sim 1 \text{ mm} \times 1 \text{ mm}$ ) and Au wire as shown in Figure 2.10 (a).

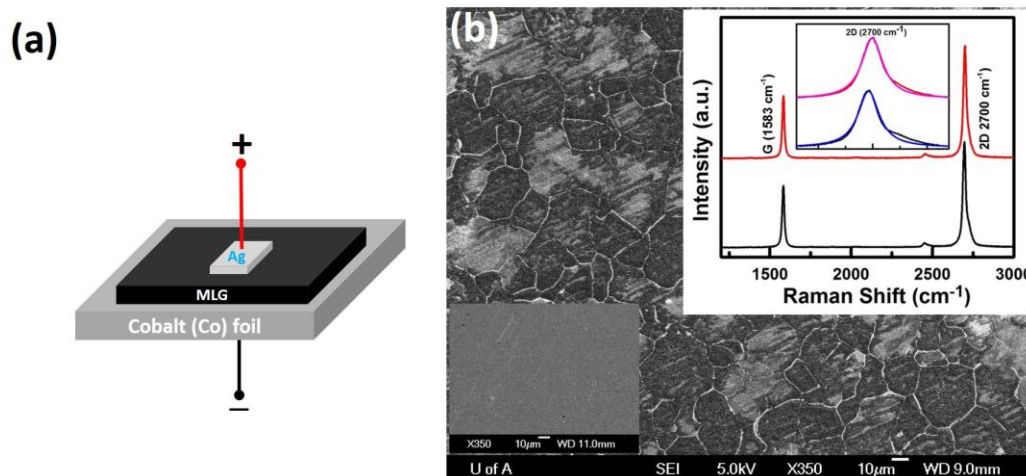


**Figure 2.10** (a) Device schematic showing bottom electrode (Co foil), MLG and top contact (Ag paste). (b) FESEM image of as grown MLG on Co foil; bottom-left inset shows bare Co foil and top-right inset shows representative Raman spectrum of as grown MLG on Co foil.

## 2.2.6 CPP MR Measurements on As-Grown MLG/Co

For all magnetotransport measurements, Lake Shore electromagnet, ARS cryo cooler, Model 332 Cryogenic Temperature Controller, and Picotest M3500A have been used. All measurement equipment are show in Figure 2.11.

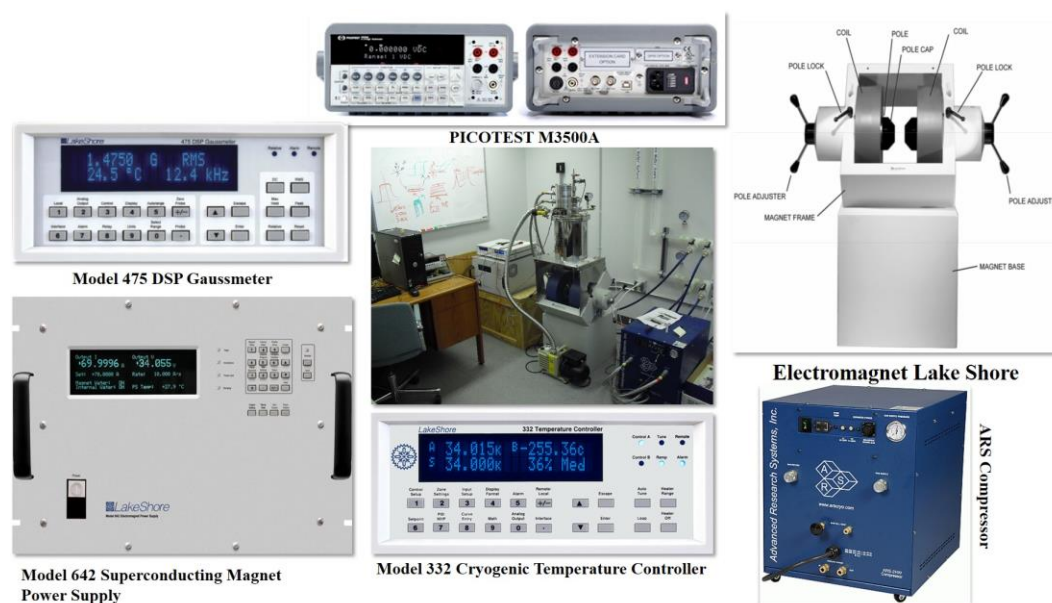


**Figure 2.11** Equipment used for CPP MR measurements.

CPP-MR measurements have been carried out in different regions as characterized above (section 2.2.3) over a wide temperature range of 8 – 300 K and magnetic field range of  $\pm 11$  kG. Each region gives rise to its own MR signature. The magnetic field is always normal to the plane (i.e. parallel to the current in the CPP configuration as shown in Figure 2.10 (a), since in this geometry magnetoresistance due to Lorentz force is eliminated. Figure 2.12 shows the typical MR plots taken from a region that shows predominantly distorted  $2D$  band (as in Figure 2.5 (c) and (d)).

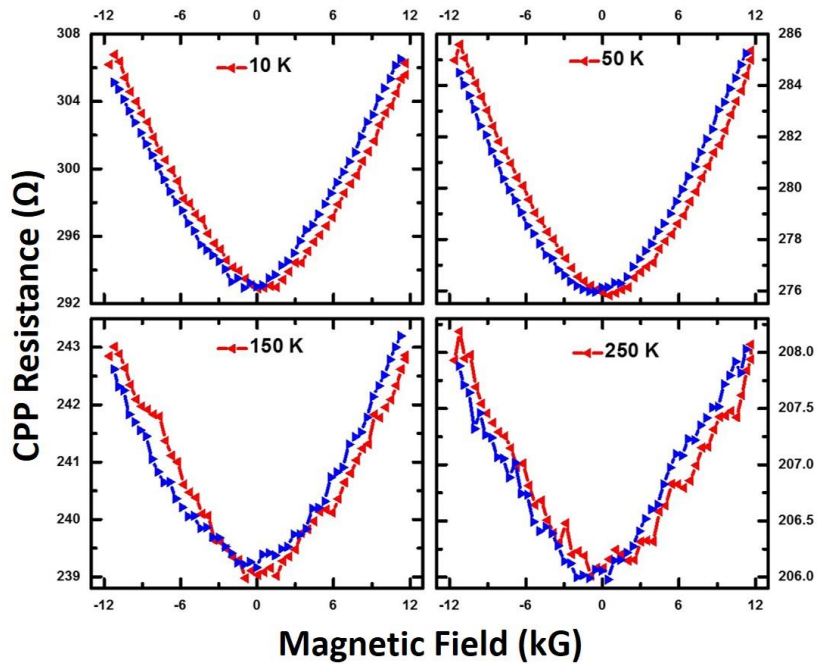


**Figure 2.12** Typical CPP MR plots taken from a region that shows predominantly distorted  $2D$  band (as in Figure 2.5 (c) and (d)).

A positive MR has been observed at all temperatures, which is consistent with previous studies on HOPG [25], [27]. CPP resistance increases by a factor of three at room temperature under an applied field of 11 kG. Figure 2.13 shows the MR response from another region which is characterized by the symmetric  $2D$  band (cases (a) and (b) in Figure 2.5). In this case a purely negative MR has been

observed (Figure 2.13). The magnitude of the negative MR =  $(R_H - R_0)/R_0$  ( $\sim 33\%$ ) is comparatively larger than the previously observed negative MR due to weak localization effect in graphitic systems [22]. The shape and switching fields are similar to the MR effects observed in as-grown MLG-Ni system [47].

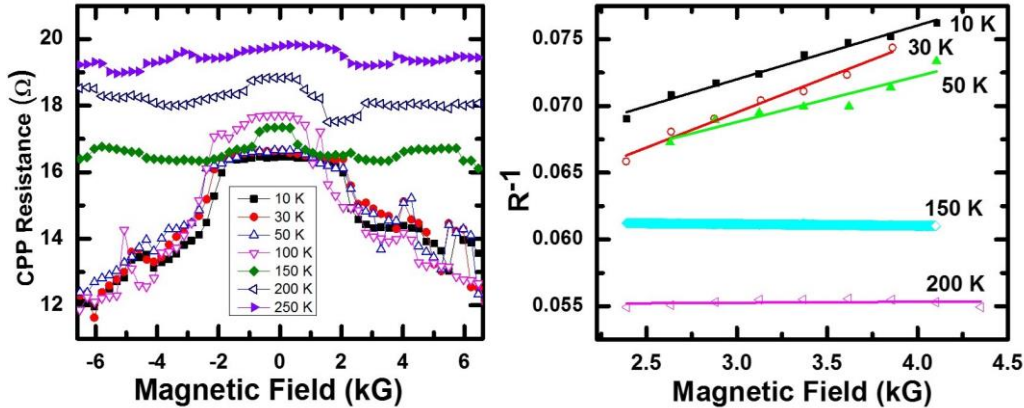


**Figure 2.13** Purely CPP negative MR response from the region characterized by the symmetrical 2D band (cases (a) and (b) in Figure 2.5).

The origin of this effect is not completely understood at this point but it has been hypothesized that CVD growth of MLG on ferromagnetic substrates can give rise to weakly coupled graphene layers (as confirmed by Raman studies) and interlayer tunnelling through these layers can give rise to large negative MR [130]–[133]. The right image of Figure 2.13 shows inverse of CPP resistance ( $R^{-1}$ ) as a function of out-of-plane magnetic field in the vicinity of the switching field of  $\sim 3$  kG. A linear trend is observed at all temperatures, which is expected from the theory of “interlayer magnetoresistance” (ILMR) [130]. Also, according to this theory, slope of  $R^{-1}$  vs.  $B$  decreases with increasing temperature, which also matches with our observation. This negative CPP MR disappears completely when field is parallel to the plane (data is not shown), which is also consistent with ILMR theory. Figure 2.14 shows the MR response from a region where  $\sim 50\%$  of the area shows symmetric 2D band (cases (a) and (b) in Figure 2.5) whereas the remaining  $\sim 50\%$  of the area shows distorted 2D Raman band (cases (c) and (d) in Figure 2.5). In this case we observe a weak positive

magnetoresistance between  $(0, \pm 5 \text{ kG})$  and then a sharp drop in the device resistance (i.e. negative MR) between  $(5 \text{ kG}, 10 \text{ kG})$ .

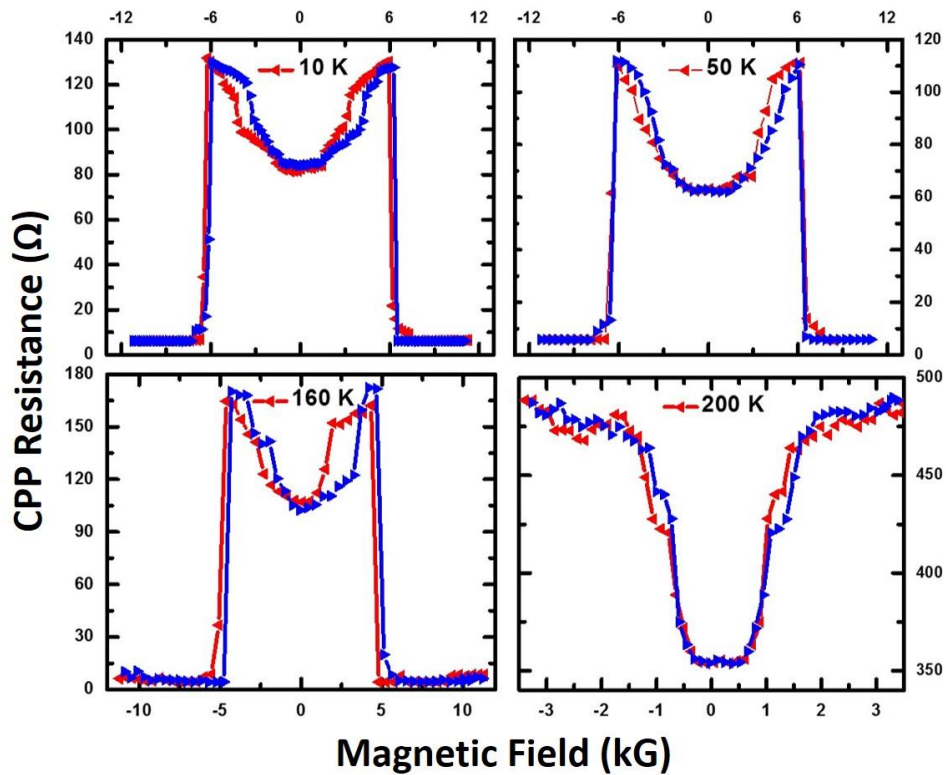


**Figure 2.14** CPP MR response from the region where  $\sim 50\%$  of the area shows symmetrical  $2D$  band, whereas the remaining  $\sim 50\%$  of the area shows distorted  $2D$  Raman band.

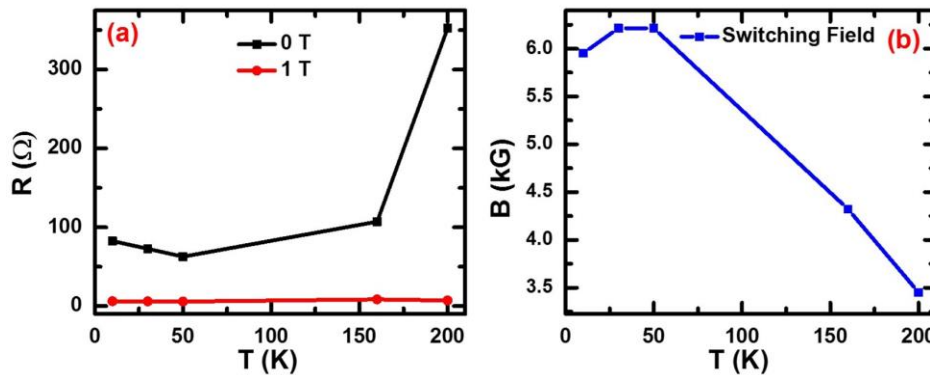


**Figure 2.15** Temperature dependence of CPP resistance ( $R$ ) and magnetic field ( $B$ ). (a)  $R$  vs.  $T$  and (b)  $B$  (switching field) vs.  $T$  of the measured sample (Figure 2.14).

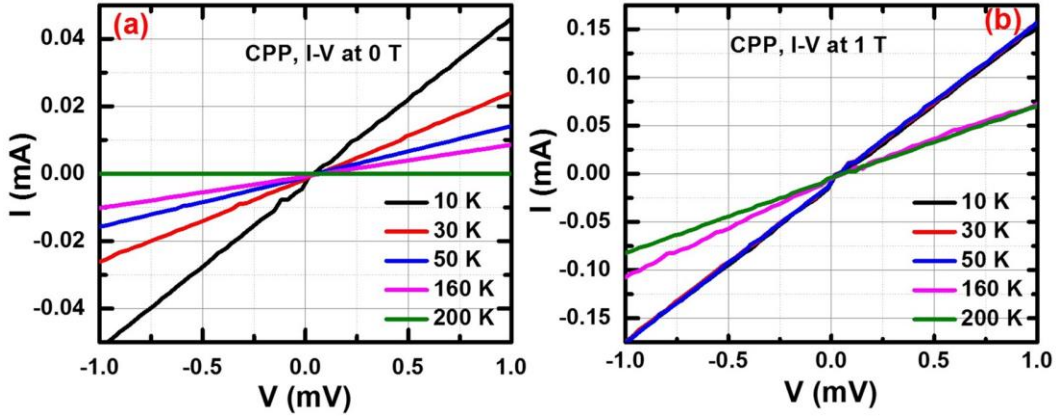


**Figure 2.16** I – V characteristics of the sample in Figure 2.14. (a) at 0 kG and (b) at 11 kG.

### 2.2.7 CPP MR of Transferred MLG on Gold (Au) electrode

We have transferred the MLG on a non-magnetic electrode (Au) using the transfer technique described above (section 2.2.2). MLG only forms a physisorption interface with Au. CPP-MR responses of these reference devices are shown in Figure 2.17. Only positive CPP MR ( $\sim 28\%$  at 8 K) has been observed and no negative MR is observed.

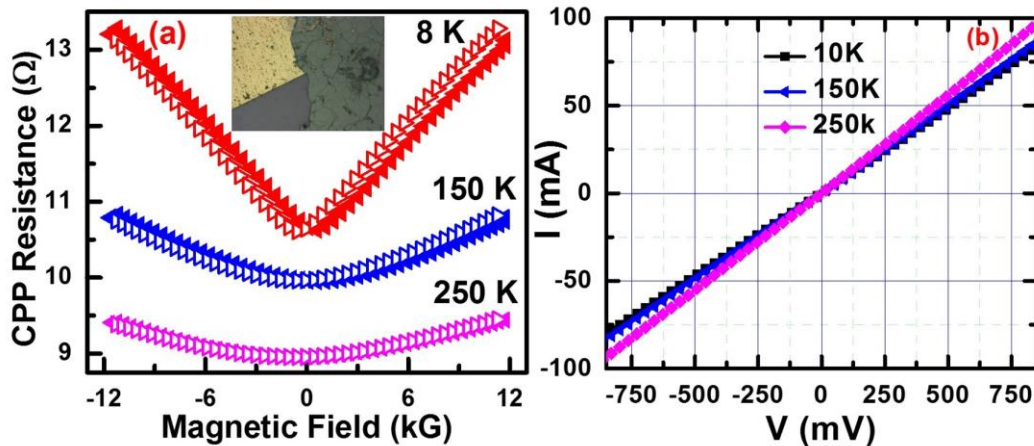


**Figure 2.17** (a) Measurements of CPP MR of (Co-grown) MLG transferred on Au electrode at 8 K, 150 K, and 250 K and inset shows optical image of transferred MLG. (b) I-V characteristic of this system at three different temperatures (8 K, 150 K, and 250 K).

### 2.2.8 Current-in-Plane (CIP) MR of Transferred MLG on Glass Substrate

In-plane resistance (Figure 2.18) of MLG (transfer process described in section 2.2.2) transferred on glass substrate shows insulating temperature dependence, which is consistent with recent observation in CVD grown MLG [134]. The transferred MLG sample showed only positive MR which weakens gradually with increasing temperature within the field range of  $\pm 11$  kG. The in-plane I-V characteristics of the transferred MLG is linear within the range of  $\pm 1.5$  V which is consistent with the resistance values observed in CIP-MR (Figure 2.19).

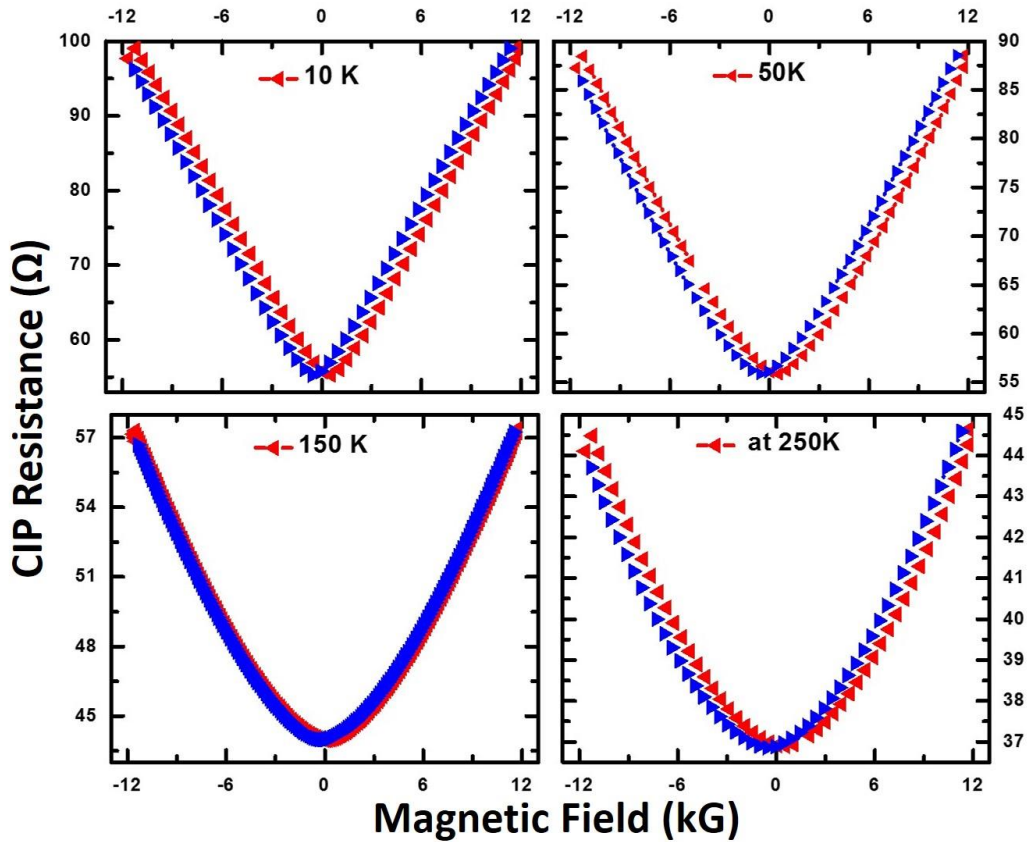


**Figure 2.18** CIP-MR of transferred MLG (Co-grown) on glass substrate.

CIP-MR ratios of MLG transferred on the glass substrate are  $\sim 80\%$ ,  $60\%$ ,  $32\%$ , and  $22\%$  at 10 K, 50 K, 150 K, and 250 K respectively.

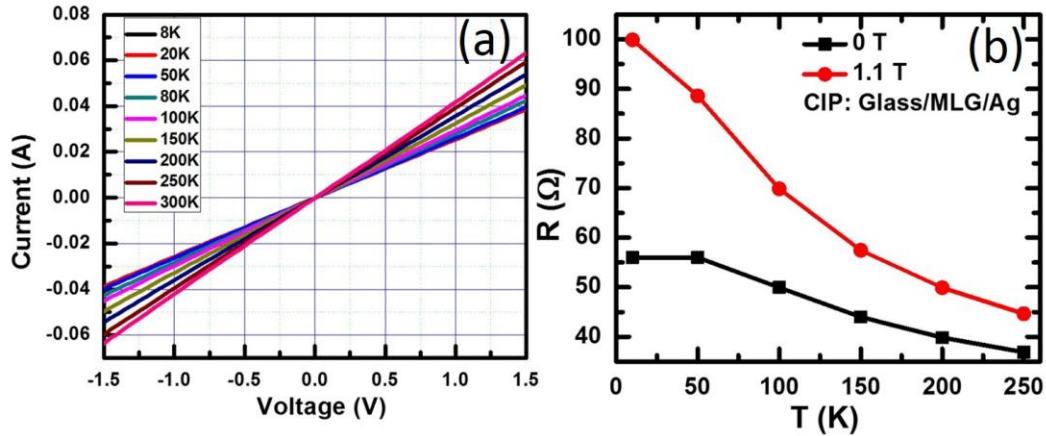


**Figure 2.19** CIP I – V characteristics and in-plane R vs. T of MLG transferred on glass. (a) In-plane I – V showing linear and insulating temperature dependence. (b) In-plane resistance showing insulating temperature dependence within the field range of  $\pm 1$  kG.

### 2.3 Result and Discussion

We have measured the current-voltage characteristics of the as-grown and the reference samples. A metallic behaviour is observed (CPP geometry) over the entire temperature range for the as-grown devices. However, the reference devices always show an insulating response. The response from the reference devices is consistent with the previous studies on c-axis transport measurements performed on graphite or multilayer graphene [22], [25]. In general, an insulating behaviour has been observed in such cases since c-axis charge transport primarily occurs via interlayer hopping. This implies that the CPP resistance in as-grown samples is dominated by the interfacial layer.

Based on the above discussions, the interfacial interaction appears to play a critical role in the observed CPP MR response. The nature of this interaction is again critically dependent on the crystal structure of the underlying Co substrate. In certain regions the interfacial interaction is such that the graphene layers formed in that region are weakly coupled to each other (symmetrical  $2D$  case). Such regions give rise to a strong negative CPP MR effect due to interlayer magnetoresistance [130], [135], [136]. In other regions the interfacial interaction

leads to formation of graphene layers that are strongly coupled to each other (asymmetrical  $2D$  case). A strong positive CPP MR is observed in these regions, which is consistent with previous studies [22]. For devices that overlap both regions, a composite MR effect (as in Figure 2.14) is observed. To understand this feature we can view the CPP resistance as a parallel combination of the interfacial resistances arising from the strongly coupled ( $R_s$ ) and weakly coupled ( $R_w$ ) regions. The effective resistance will be essentially dominated by the smaller of these two resistances. We note that  $R_s(B)$  exhibits a positive MR whereas  $R_w(B)$  exhibits negative MR. At low magnetic field  $R_s$  is smaller and the net CPP MR will have the shape of  $R_s(B)$  i.e. we expect to see a positive MR at low fields. Beyond a certain critical magnetic field  $R_s$  becomes larger than  $R_w$  and in this region net CPP MR will have the shape of  $R_w(B)$  i.e. negative MR. This is exactly what we observe in Figure 2.14.

## 2.4 Conclusion

Thus in conclusion we have reported CPP MR measurements performed on MLG as-grown on ferromagnetic Co substrate. Strong magnetoresistance effects have been observed even at room temperatures. The origin of the MR effect lies at the graphene-Co interfacial interaction. This interaction can be used as a handle to realize tailor-made MR responses, which may have technological applications in magnetic data storage and information processing. Further insight can be obtained by performing a thickness-dependent experiment, which is reserved for future study.

## 3 High Density Integration of MWCNT Spin Valves<sup>1</sup>

### 3.1 Introduction

Spin-based non-volatile memory has recently attracted significant attention since it can potentially emerge as a “universal memory” [138]. The basic memory cell has a “spin valve” configuration in which a non-magnetic material (generally a tunnel barrier) is sandwiched between two ferromagnetic electrodes. The resistance state of this device is “bistable”, which can be used to store binary information. Switching between these two states is achieved by controlling the relative magnetization of the contact ferromagnets, which changes spin-dependent transmission coefficients of the charge carriers at the contacts. In most cases, when the magnetizations of the ferromagnetic contacts are parallel to each other, device resistance is low and when they are anti-parallel device resistance is high. Although in some cases an “inverse” spin valve behavior has been observed [34] where the resistance is high (low) when the contacts are parallel (anti-parallel). Spin valve memories (also known as magnetic random access memories or MRAM) currently available in the market (e.g. Freescale/Everspin Technologies<sup>2</sup>) typically employ a tunnel barrier as the non-magnetic spacer. Unfortunately this configuration is not scalable to high bit densities due to the following technological bottlenecks: (1) Simultaneous realization of small resistance-area (RA) product and high on-off ratio over the entire chip is difficult for tunnel junctions due to technological issues such as pinhole shorts and dielectric breakdown. (2) Ferromagnets, scaled to small dimensions, are prone to random flip in magnetization even at ambient temperature (superparamagnetism). This leads to increased soft-error rate. Due to these reasons current spin based memory chips (as marketed by EVERSPIN Technologies) exhibit poor storage capacities ranging from 256 kb to 16 Mb (chip MR4A16BCMA35). Multi-walled carbon

---

<sup>1</sup> This chapter has been published in ref. [137].

<sup>2</sup> <http://www.freescale.com>, <http://www.everspin.com>

nanotubes (MWCNTs) are promising material for spin based memory applications since they offer long spin relaxation lengths and time due to very weak spin-orbit and hyperfine interaction [139]–[141]. This translates to well-separated resistance state in MWCNT spin valves, which is desirable for memory devices. Even though single MWCNT spin valves has been demonstrated [139]–[141] high density integration of such memory elements are largely underdeveloped [89], [90], [142] . One possible method is to fabricate the spin valve memory cells in the highly ordered pores on an anodic alumina (AAO) template. The device schematic is shown in Figure 3.5. Such method has shown poor spin valve response in the past [142] mainly due to long tube length and/or poor tube quality. In this work we report spin valve signal observed in short channel MWCNTs embedded in AAO, which shows spin relaxation length of 0.28  $\mu\text{m}$  at 8 K.

## **3.2 Experimental Methods**

### **3.2.1 Fabrication of Nanoporous Anodic Aluminum Oxide (AAO) Template**

Nanoporous anodic aluminum oxide (AAO) template has been fabricated using a standard technique (Figure 3.1) discussed in detail in ref. [143]. We employ an electrochemical self-assembly technique to fabricate a hexagonally ordered array of cylindrical nanopores on an aluminum substrate. We start with high purity unpolished and annealed aluminum (99.997%, Alfa Aesar) foil with thickness  $\sim 250 \mu\text{m}$ . These unpolished samples are subjected to chemical polishing [143] using 15 parts of 68% nitric acid and 85 parts of 85% phosphoric acid for 5 min at 85  $^{\circ}\text{C}$ . Next, the samples are neutralized in 1 M sodium hydroxide for 20 min. Finally, we perform multistep anodization [143] on these chemical polished samples using 3% oxalic acid and 40 V dc at room temperature. Final step of anodization is carried out for 5 minutes, which produces pore length  $\sim 1 \mu\text{m}$ . Pore density is  $\sim 10^{10}/\text{cm}^2$  as shown in the inset of Figure 3.2 and can be controlled by adjusting the self-assembly parameters. There exists a thin continuous layer of alumina barrier between pore bottom and aluminum substrate.

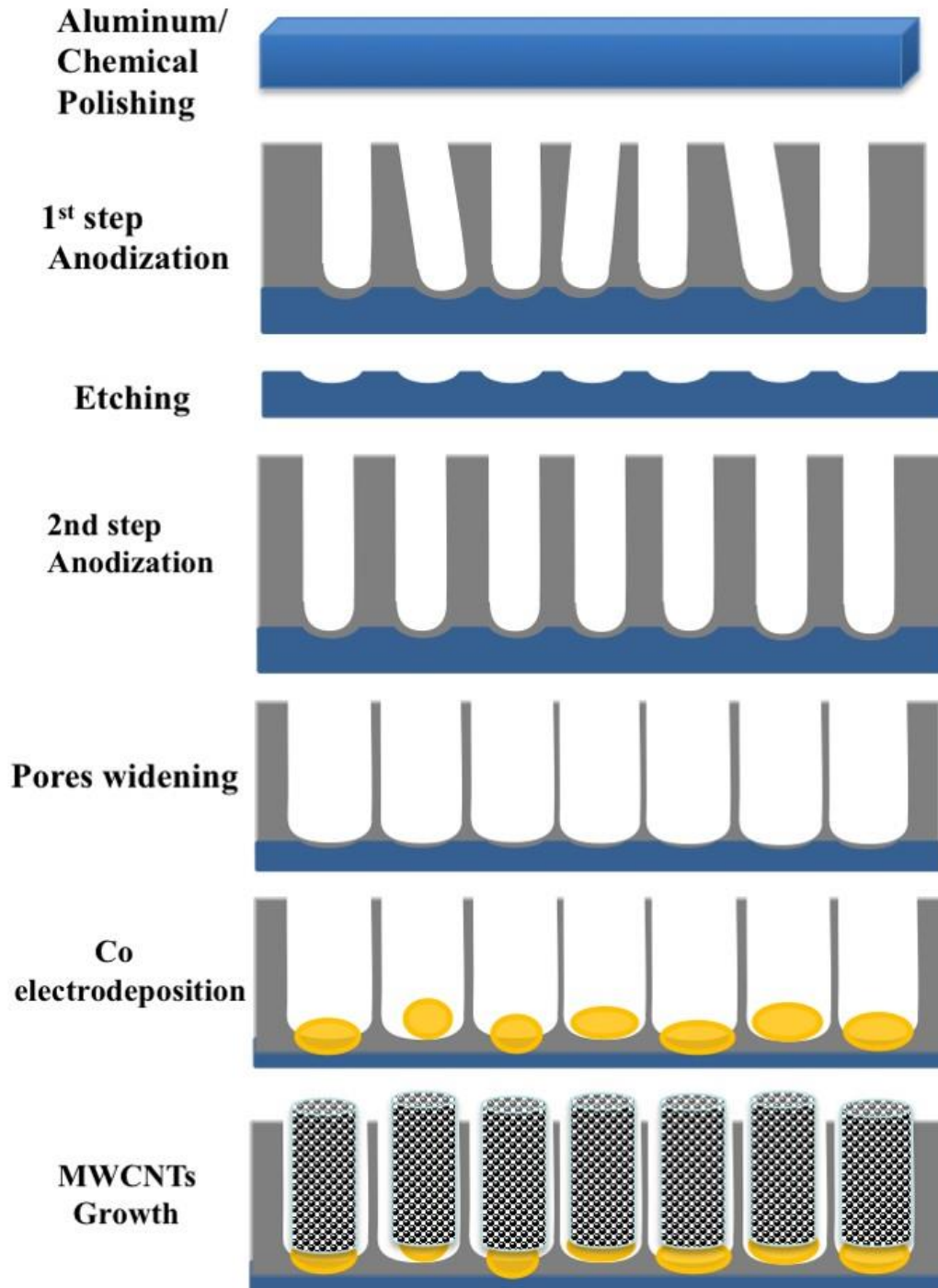


**Figure 3.1** Process flow of fabrication of nanoporous AAO template and growth of MWCNT array.

The barrier layer is thinned and the pores are widened by etching in 5%  $H_3PO_4$  for 60 min. In some regions the barrier layer is completely removed, whereas in

other regions thin (~ 10 nm) barrier layer is still present. The pores are partially filled with cobalt catalyst by electrochemical deposition using a 5%  $\text{CoSO}_4 \cdot 7\text{H}_2\text{O}$  solution stabilized with 2%  $\text{H}_3\text{BO}_3$  under 20V ac and 250Hz [144]. The field emission scanning electron microscopic (FESEM) image of electrodeposited Co catalyst is shown in Figure 3.2. Due to the non-uniformity of the barrier layer, the thickness of the electrochemically deposited Co is non-uniform.

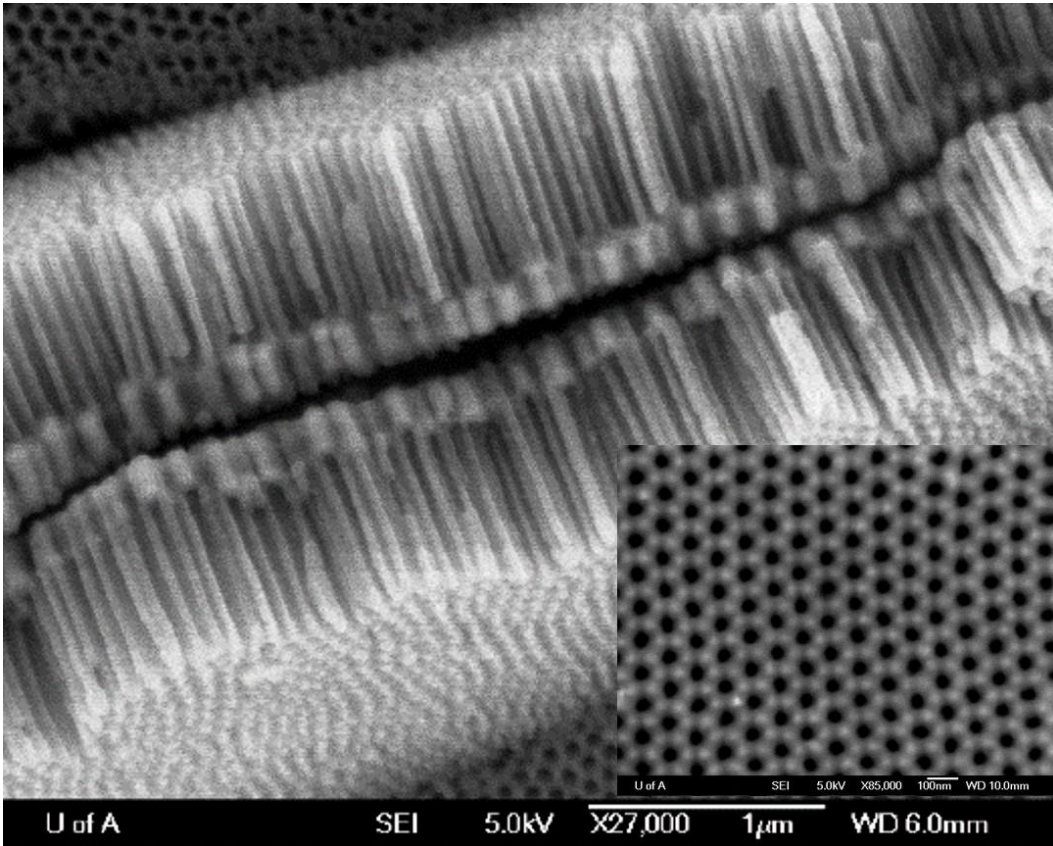


**Figure 3.2** FESEM image of electrochemically deposited Co at the bottom of the nanopores and the inset shows a two-dimensional array of well-regimented nanopores.

### 3.2.2 Fabrication of Spin Valve Using MWCNT as Spacer Layer

Multi-walled carbon nanotubes are grown in a commercial Tystar chemical vapor deposition chamber. Typical process flow includes (a) catalyst (Co) deposited nanoporous alumina template load, (b) furnace purge, (c) temperature ramp and hydrogen reduction, (d) CNT growth, (e) cooling, and (f) unloading [145], [146].

Ethylene ( $C_2H_2$ ) is used as a carbon precursor during CNT growth at  $650\text{ }^\circ\text{C}$ . Figure 3.3 shows the FESEM image of as-grown CNTs in the nanopores. Overgrown CNTs on the surface of the AAO nanopores are removed by ultrasonic treatment in acetone [147], [148]. Figure 3.4 shows the top surface after the treatment. Since the Co layer is  $\sim 300\text{ nm}$  thick, the length of the MWCNT is  $\sim 700\text{ nm}$ . The bottom ferromagnet (Co) serves as an electrical contact to the CNTs. A second ferromagnetic layer (Ni) of  $\sim 80\text{ nm}$  thickness is deposited by magnetron sputtering on the top which completes the spin valve structure. Ni sputtering is done only at few areas on the top surface using a mechanical mask. Electrical contacts were made with silver paste and gold wire. Silver paste was used to connect gold wire on the top of patterned Ni pad. Spreading of silver paste over the Ni pad was avoided by mixing silver paste in an appropriate solvent.

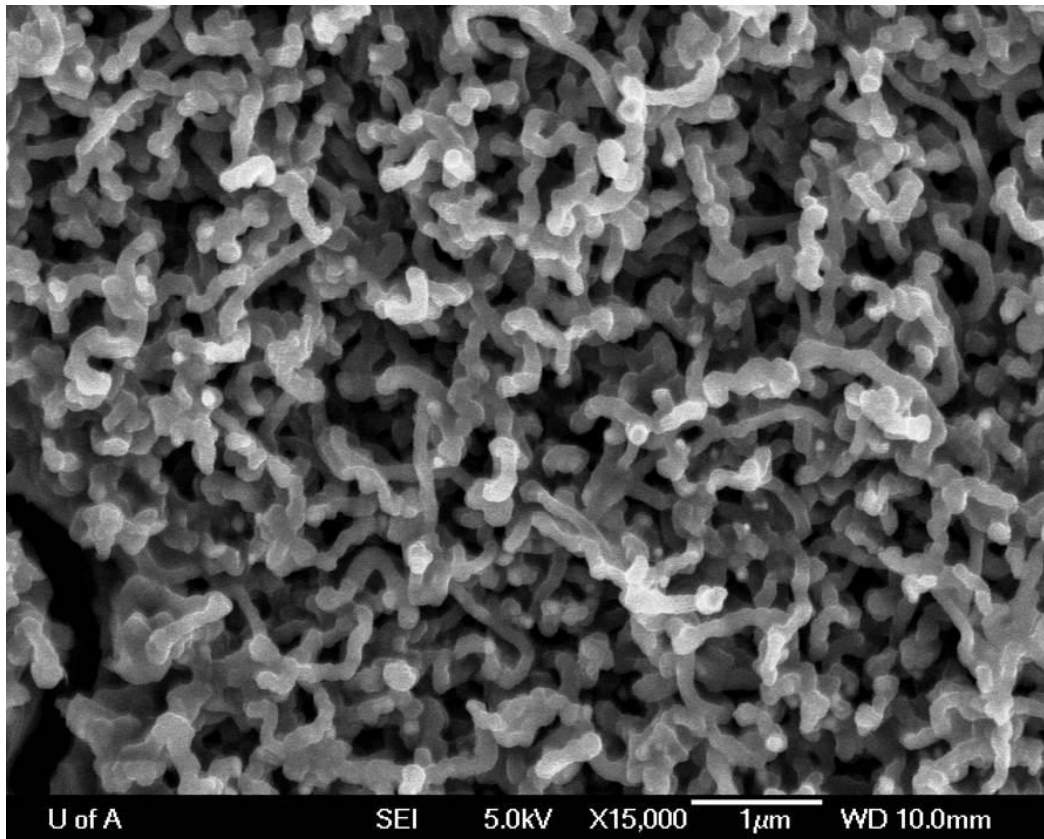


**Figure 3.3** FESEM image of as grown CNTs in AAO. Overgrown CNTs covers the top surface.

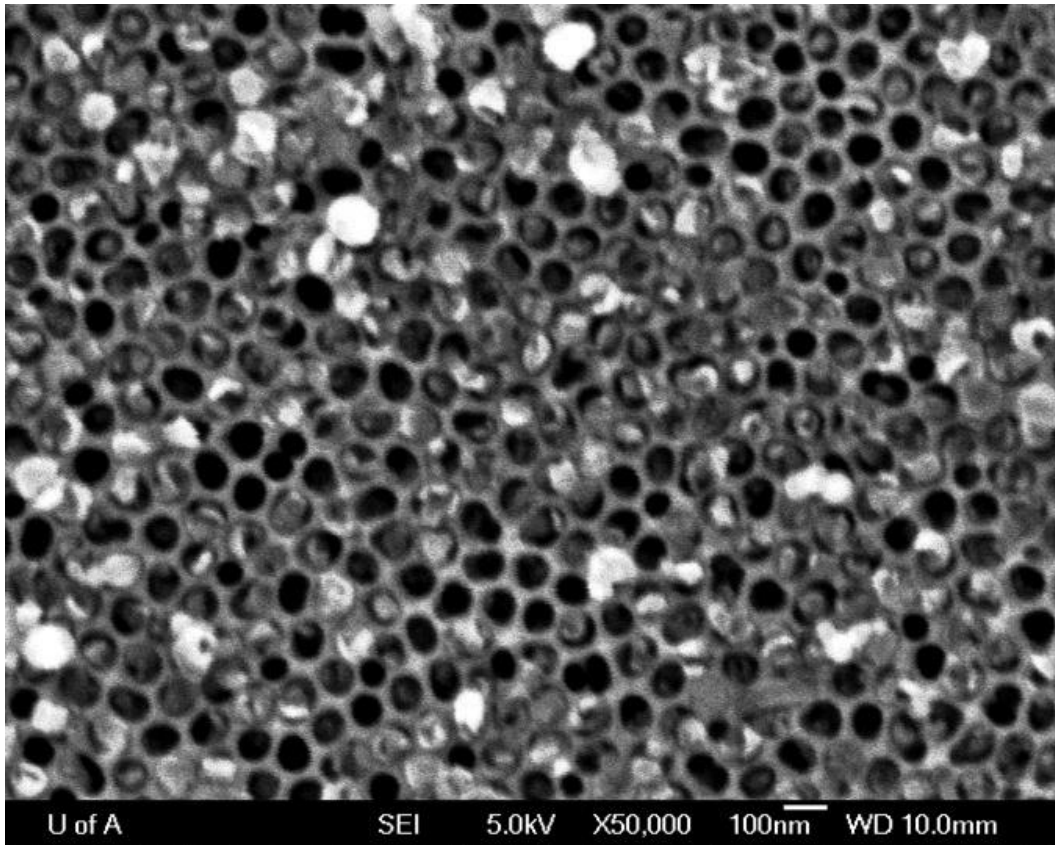


**Figure 3.4** FESEM image of CNTs after removing the overgrowth by ultrasonication.

Spin valve schematic is shown in Figure 3.5.

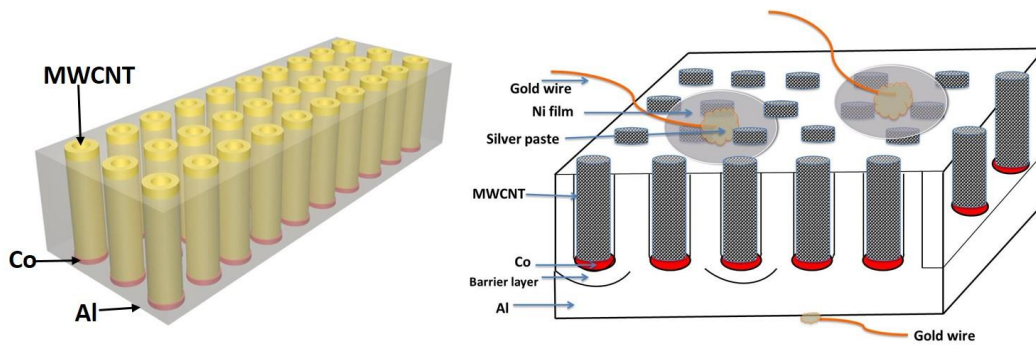


**Figure 3.5** Schematic diagram of a CNT spin valve device. The CNTs are hosted in an insulating porous alumina template. The barrier layer at Al/Al<sub>2</sub>O<sub>3</sub> interface is partially removed and only a fraction of CNTs are electrically contacted from both sides. The magnetic field is applied along the axis of the tube.

### 3.2.3 Characterization of MWCNT Using Raman Spectroscopy

Raman spectroscopy has been performed by Nicolet Almega XR micro-Raman analysis system. Laser wavelength of 532 nm and 24 mW power have been used for this spectroscopic study. Details of this study are provided in the next section.

### 3.2.4 Spin-valve Characterization

Model 642-electromagnet power supply and Cryotronics 332 Controller from Lakeshore have been used as an electromagnet current source and temperature controller respectively. The magnetic field in the range [+6000 Oe to -6000 Oe] is applied parallel to the nanowire axis. All measurements have been performed in the range [8K-40K]. Picotest M3500A multimeter has been used to extract directly the resistance of the device. Each resistance value is the average of 20 readings. A 475 DSP gauss meter has been used to record the magnetic field values. A Lab View VI is created to synchronize with all measurement equipment for data acquisition. Details of this study are provided in the next section.

## 3.3 Result and Discussion

Characteristic Raman spectrum was found in as-grown MWCNT as well as after removing the overgrown MWCNT. As expected, Raman spectrum of the MWCNTs shows (Figure 3.6) typical graphitic ( $G = 1594 \text{ cm}^{-1}$ ) and defective ( $D = 1335 \text{ cm}^{-1}$ ) peaks. There was no noticeable difference in peak position and shape in the Raman spectrum before and after cutting overgrown MWCNTs. The resistance of a spin valve depends on the relative magnetization orientations of the ferromagnetic contacts. The spin valve signal  $\Delta R/R$  is defined as follows [44]:

$$\frac{\Delta R}{R} = \frac{R_{AP} - R_P}{R_P} \quad \text{Equation 3.1}$$

where  $R_{AP}$  and  $R_P$  denote the device resistance when the magnetizations of the two ferromagnetic contacts are antiparallel (AP) and parallel (P), respectively [34],[149]. The coercivity of the Ni thin film is typically  $\sim 200$  Oe and the

coercivity of Co nanorod (60 nm in diameter and 200–300 nm in length) is  $\sim 4000$  Oe at low temperature [34].

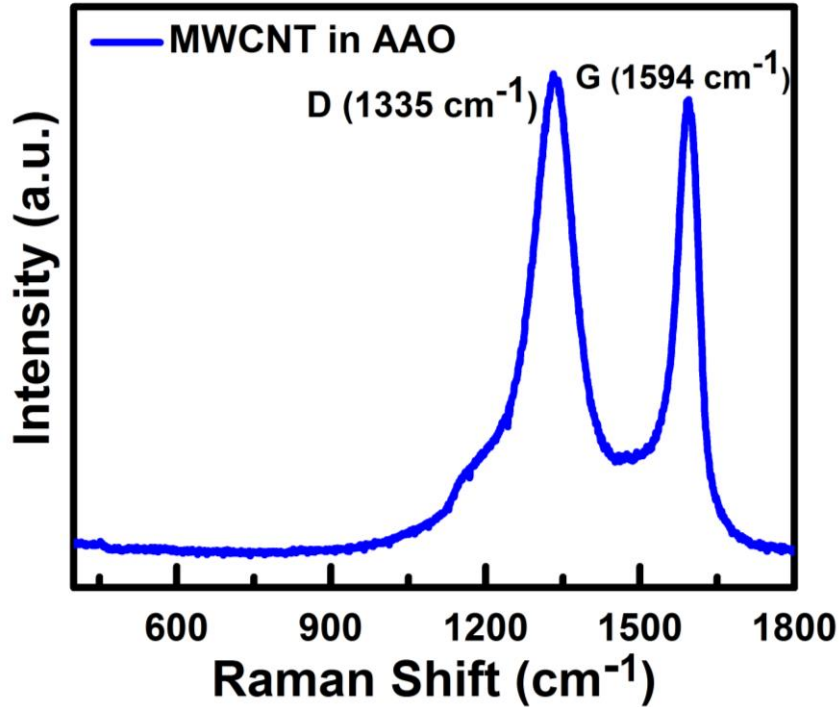


**Figure 3.6** Typical Raman spectra of as-grown MWCNTs.

While decreasing the magnetic field from +6000 Oe to -6000 Oe (Figure 3.7) both ferromagnets (Co nanorod and Ni thin film) are magnetized in the same direction. When the magnetic field reaches at  $\sim -200$  Oe, Ni thin film switches magnetization. Therefore we observe a jump in the device resistance at  $\sim -200$  Oe. When the magnetic field reaches  $\sim -4000$  Oe then magnetization of Co nanorods flips. Now the magnetization is parallel and the device resistance falls back to its original value. So we get high resistance in the field range of -200 Oe to -4000 Oe. Similarly when we sweep the magnetic field in the reverse direction we observe a similar jump in device resistance in the window of  $\sim 200$  to  $\sim 4000$  Oe. Resistance is in the range of 5 to 12  $\Omega$  which indicate that most of the synthesized CNTs are metallic. This also implies that many ( $\sim 10^8$ ) spin valves are connected in parallel. Similar geometry has been reported in the past [34]. We estimate the

resistance of a single spin valve device to be  $\sim 10^9 \Omega$  which is the typical resistance value of single MWCNT spin valves [139], [141].

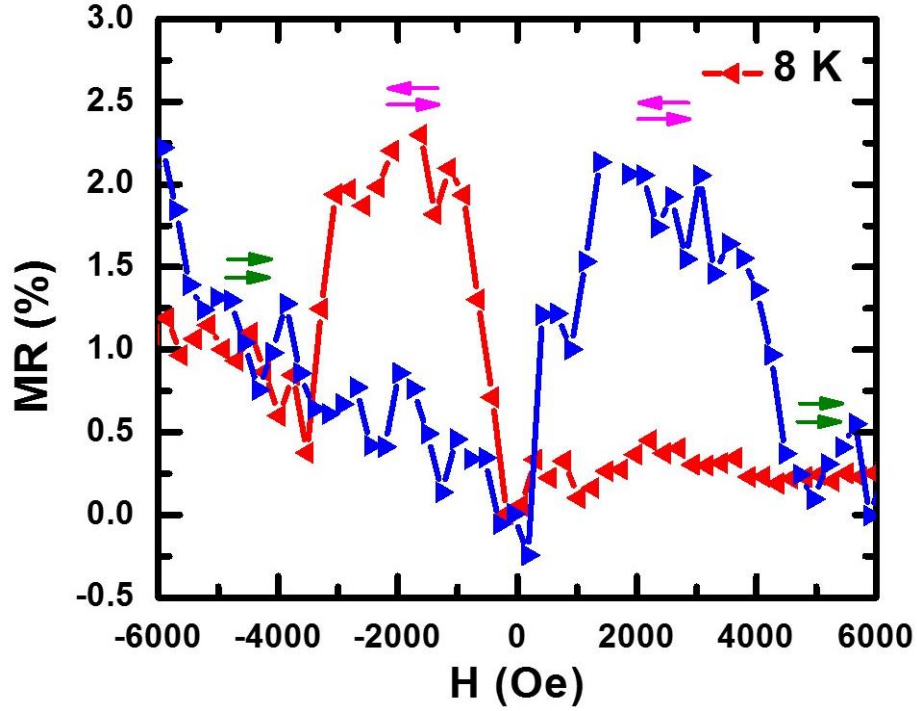


**Figure 3.7** Spin valve effect observed in Ni-MWCNT-Co spin valve at 8K.

Spin-valve signal disappears as temperature is increased as shown in Figure 3.8. Using the available experimental data it is possible to extract a lower bound of spin relaxation length in MWCNTs. Applying modified Jullière<sup>3</sup> formula [34], [35], [150] at the “detecting” interface, we get

$$\frac{\Delta R}{R} = \frac{2P_1 e^{-d/L_s} P_2}{1 - P_1 e^{-d/L_s} P_2} \quad \text{Equation 3.2}$$

where  $P_1$  and  $P_2$  are the spin polarizations of the top (Ni) and bottom (Co) contact

<sup>3</sup> In the Jullière model [150] the transmission through the insulating interlayer is assumed to be independent of the electron energy but proportional to the DOS at the Fermi level  $E_F$  of both contacts. Spin-flip processes at the interfaces and in the interlayer are neglected.

respectively,  $d$  is the width of the spacer layer (MWCNT), and  $L_s$  is the spin relaxation length. This model has been used in ref. [151] to calculate the spin relaxation length  $L_s$  in other materials such as organics. This model ignores any possible loss of spin polarization at the interface between the MWCNT and the ferromagnetic contact and therefore the estimated  $L_s$  indicates the lower bound of spin relaxation length.

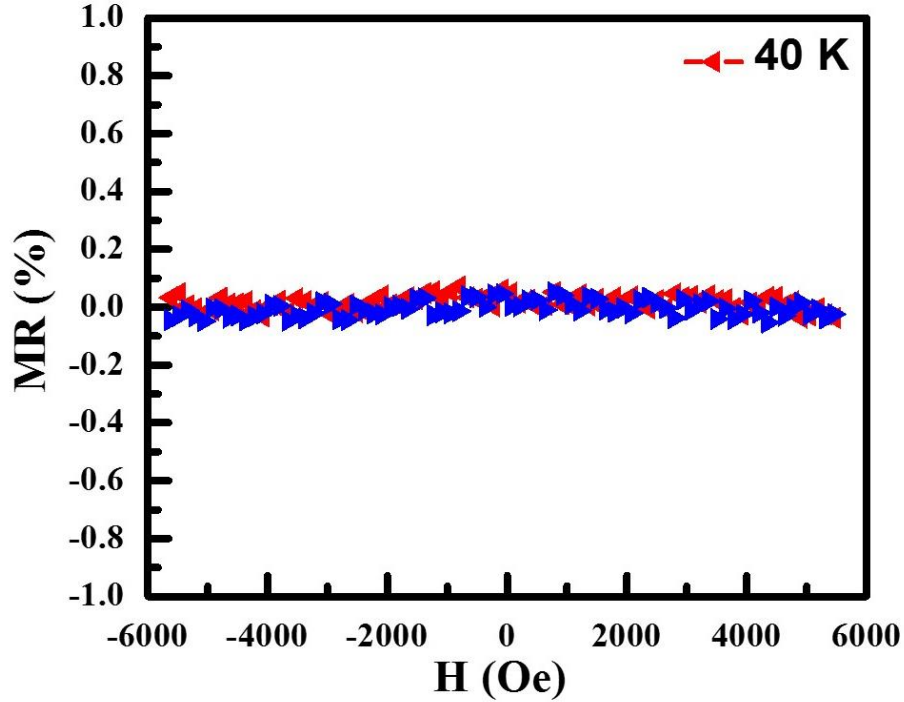


**Figure 3.8** Absence of spin valve effect in Ni-MWCNT-Co device at 40K.

From Figure 3.7,  $\Delta R/R$  (at 8 K) is 0.023 and using  $P_1 = 0.33$ ,  $P_2 = 0.42$  [35] and  $d = 700$  nm, we find the spin diffusion length  $L_s \sim 0.28 \mu\text{m}$ .

### 3.4 Conclusion

In this work we have demonstrated an array of vertically standing MWCNT spin valves synthesized in the pores of an anodic alumina template. All pores are short length ( $< 1\mu\text{m}$ ), parallel to each other and electrically isolated via alumina walls. Spin relaxation length of  $\sim 0.28 \mu\text{m}$  has been observed at 8 K, which can be

further increased by improving the quality of the MWCNTs. In a previous work, the spin-flip scattering length of  $\sim 130$  nm was reported [42]. In this work an individual MWCNT of  $\sim 10 - 40$  nm in diameter contacted by Co electrodes at 4 K was measured. In another individual MWCNT based spin valve device (LSMO – individual MWCNT – LSMO), spin relaxation length was observed up to  $50 \mu\text{m}$  [44] presumably due to the highly spin-polarized LSMO contacts. All these early work involved individual MWCNT and required precise lithography. Ref. [88] reported highly ordered nanoporous template (AAO) to fabricate MWCNT spin valve array. A calculated spin relaxation length of  $2 \mu\text{m}$  at temperatures up to 40 K was observed, even though quality of spin valve signal was extremely poor. Here we have demonstrated spin valve devices fabricated from aligned arrays of MWCNTs, allowing relatively simple fabrication and demonstrating spin relaxation length of  $\sim 0.28 \mu\text{m}$ . Our calculated spin relaxation length is higher than 130 nm reported in ref. [42] which used only Co electrodes, and lower than  $50 \mu\text{m}$  [44] where highly spin polarized LSMO was used as ferromagnetic electrodes. Using SWCNT, further reducing the length of spacer layer, and better ferromagnet-CNT contact can potentially increase spin relaxation length.

## 4 Summary and Outlook

In summary, we have explored various magnetoresistance (MR) effects in carbon based nanostructures such as multilayer graphene (MLG) and multiwall carbon nanotubes. First, c-axis magnetoresistance effects have been observed in multilayer graphene (MLG) as-grown on cobalt (Co) foil using chemical vapor deposition (CVD). Purely positive MR is found in the case when constituent graphene layers in MLG are strongly coupled ( $2D$  is asymmetric in Raman spectrum). Negative MR is observed in the case when the constituent graphene layers in MLG are weakly coupled ( $2D$  is symmetrical in Raman spectrum). A composite MR response, containing both positive and negative MR behavior, is observed in the case when MLG shows an equal distribution of symmetrical and asymmetrical  $2D$  peak in Raman spectrum. Positive c-axis MR has been found in transferred (Co-grown) MLG on gold (Au) electrode, fabricated on  $\text{SiO}_2/\text{Si}$  substrate. A strong CIP (current-in-plane) MR has also been observed in Co-grown samples. A qualitative explanation of the MR effects has been provided in Chapter 2. For a deeper understanding of observed MR effects it is necessary to conduct thickness dependence study of the MR signals, which has been reserved for future work.

Next, we have also demonstrated an array of vertically standing multi-wall carbon nanotube (MWCNT) spin valves synthesized in a nanoporous anodic alumina template (AAO). All nanopores are parallel to each other and electrically isolated via alumina walls, and short in length ( $< 1 \mu\text{m}$ ). Spin relaxation length of  $\sim 0.28 \mu\text{m}$  has been observed at 8K. Improving the quality of MWCNTs, FM-MWCNTs contacts, and reducing scattering by using single-wall CNTs can further increase the spin relaxation length. We note that carbon nanotubes are promising candidates for various spintronics application. Recent theory work [152] has predicted that single-walled carbon nanotubes (CNTs) when wrapped with single stranded deoxyribonucleic acid (DNA) can behave like a one dimensional spin

polarized conductor. The presence of helicoidal fields and Rashba spin-orbit coupling results in spin filtering in this chiral nano structure [152]. Investigation of such geometries are beyond the scope of this thesis and are currently being pursued by other members of our group.

## References

- [1] N. W. Ashcroft and N. D. Mermin, *Solid State Physics*. New York; London: Harcourt College Publishers, 1976.
- [2] C. Chappert, A. Fert, and F. N. Van Dau, “The emergence of spin electronics in data storage,” *Nat. Mater.*, vol. 6, no. 11, pp. 813–823, Nov. 2007.
- [3] T. R. McGuire and R. I. Potter, “Anisotropic magnetoresistance in ferromagnetic 3d alloys,” *IEEE Trans. Magn.*, vol. 11, no. 4, pp. 1018–1038, 1975.
- [4] P. Grünberg, R. Schreiber, Y. Pang, M. B. Brodsky, and H. Sowers, “Layered Magnetic Structures: Evidence for Antiferromagnetic Coupling of Fe Layers across Cr Interlayers,” *Phys. Rev. Lett.*, vol. 57, no. 19, pp. 2442–2445, Nov. 1986.
- [5] M. N. Baibich, J. M. Broto, A. Fert, F. N. Van Dau, F. Petroff, P. Etienne, G. Creuzet, A. Friederich, and J. Chazelas, “Giant Magnetoresistance of (001)Fe/(001)Cr Magnetic Superlattices,” *Phys. Rev. Lett.*, vol. 61, no. 21, pp. 2472–2475, Nov. 1988.
- [6] T. Miyazaki and N. Tezuka, “Giant magnetic tunneling effect in Fe/Al<sub>2</sub>O<sub>3</sub>/Fe junction,” *J. Magn. Magn. Mater.*, vol. 139, no. 3, pp. L231–L234, Jan. 1995.
- [7] S. S. P. Parkin, C. Kaiser, A. Panchula, P. M. Rice, B. Hughes, M. Samant, and S.-H. Yang, “Giant tunnelling magnetoresistance at room temperature with MgO (100) tunnel barriers,” *Nat. Mater.*, vol. 3, no. 12, pp. 862–867, Dec. 2004.
- [8] R. von Helmolt, J. Wecker, B. Holzapfel, L. Schultz, and K. Samwer, “Giant negative magnetoresistance in perovskitelike La<sub>2/3</sub>Ba<sub>1/3</sub>MnO<sub>x</sub> ferromagnetic films,” *Phys. Rev. Lett.*, vol. 71, no. 14, pp. 2331–2333, Oct. 1993.
- [9] S. Jin, T. H. Tiefel, M. McCormack, R. A. Fastnacht, R. Ramesh, and L. H. Chen, “Thousandfold Change in Resistivity in Magnetoresistive La-Ca-Mn-O Films,” *Science*, vol. 264, no. 5157, pp. 413–415, Apr. 1994.
- [10] J. Nickel, *Magnetoresistance Overview*. Hewlett-Packard Laboratories, Technical Publications Department, 1995.

- [11] K. S. Novoselov, V. I. Fal'ko, L. Colombo, P. R. Gellert, M. G. Schwab, and K. Kim, "A roadmap for graphene," *Nature*, vol. 490, no. 7419, pp. 192–200, Oct. 2012.
- [12] W. Y. Kim and K. S. Kim, "Prediction of very large values of magnetoresistance in a graphene nanoribbon device," *Nat. Nanotechnol.*, vol. 3, no. 7, pp. 408–412, Jul. 2008.
- [13] F. Muñoz-Rojas, J. Fernández-Rossier, and J. J. Palacios, "Giant Magnetoresistance in Ultrasmall Graphene Based Devices," *Phys. Rev. Lett.*, vol. 102, no. 13, p. 136810, Apr. 2009.
- [14] J. Bai, R. Cheng, F. Xiu, L. Liao, M. Wang, A. Shailos, K. L. Wang, Y. Huang, and X. Duan, "Very large magnetoresistance in graphene nanoribbons," *Nat. Nanotechnol.*, vol. 5, no. 9, pp. 655–659, Sep. 2010.
- [15] A. L. Friedman, J. L. Tedesco, P. M. Campbell, J. C. Culbertson, E. Aifer, F. K. Perkins, R. L. Myers-Ward, J. K. Hite, C. R. Eddy, G. G. Jernigan, and D. K. Gaskill, "Quantum Linear Magnetoresistance in Multilayer Epitaxial Graphene," *Nano Lett.*, vol. 10, no. 10, pp. 3962–3965, Oct. 2010.
- [16] J. Lu, H. Zhang, W. Shi, Z. Wang, Y. Zheng, T. Zhang, N. Wang, Z. Tang, and P. Sheng, "Graphene Magnetoresistance Device in van der Pauw Geometry," *Nano Lett.*, vol. 11, no. 7, pp. 2973–2977, Jul. 2011.
- [17] M. M. Parish and P. B. Littlewood, "Non-saturating magnetoresistance in heavily disordered semiconductors," *Nature*, vol. 426, no. 6963, pp. 162–165, Nov. 2003.
- [18] A. A. Abrikosov, "Quantum magnetoresistance," *Phys. Rev. B*, vol. 58, no. 5, pp. 2788–2794, Aug. 1998.
- [19] A. A. Abrikosov, "Quantum linear magnetoresistance," *EPL Europhys. Lett.*, vol. 49, no. 6, p. 789, Mar. 2000.
- [20] A. H. Castro Neto, F. Guinea, N. M. R. Peres, K. S. Novoselov, and A. K. Geim, "The electronic properties of graphene," *Rev. Mod. Phys.*, vol. 81, no. 1, pp. 109–162, Jan. 2009.
- [21] J. Hu and T. F. Rosenbaum, "Classical and quantum routes to linear magnetoresistance," *Nat. Mater.*, vol. 7, no. 9, pp. 697–700, Sep. 2008.
- [22] Z.-M. Liao, H.-C. Wu, S. Kumar, G. S. Duesberg, Y.-B. Zhou, G. L. W. Cross, I. V. Shvets, and D.-P. Yu, "Large Magnetoresistance in Few Layer

- Graphene Stacks with Current Perpendicular to Plane Geometry,” *Adv. Mater.*, vol. 24, no. 14, pp. 1862–1866, 2012.
- [23] K. S. Novoselov, Z. Jiang, Y. Zhang, S. V. Morozov, H. L. Stormer, U. Zeitler, J. C. Maan, G. S. Boebinger, P. Kim, and A. K. Geim, “Room-Temperature Quantum Hall Effect in Graphene,” *Science*, vol. 315, no. 5817, pp. 1379–1379, Mar. 2007.
- [24] C. R. Dean, A. F. Young, P. Cadden-Zimansky, L. Wang, H. Ren, K. Watanabe, T. Taniguchi, P. Kim, J. Hone, and K. L. Shepard, “Multicomponent fractional quantum Hall effect in graphene,” *Nat. Phys.*, vol. 7, no. 9, pp. 693–696, Sep. 2011.
- [25] H. Kempa, P. Esquinazi, and Y. Kopelevich, “Field-induced metal-insulator transition in the c-axis resistivity of graphite,” *Phys. Rev. B*, vol. 65, no. 24, p. 241101, May 2002.
- [26] W. Zhi-Ming, X. Ding-Yu, Z. Shi-Yuan, X. Qing-Yu, M. VanBael, and D. You-Wei, “Magnetic-Field-Induced Semimetal-Insulator-like Transition in Highly Oriented Pyrolytic Graphite,” *Chin. Phys. Lett.*, vol. 24, no. 1, p. 199, Jan. 2007.
- [27] D. V. Khveshchenko, “Magnetic-Field-Induced Insulating Behavior in Highly Oriented Pyrolytic Graphite,” *Phys. Rev. Lett.*, vol. 87, no. 20, p. 206401, Oct. 2001.
- [28] D. V. Khveshchenko, “Ghost Excitonic Insulator Transition in Layered Graphite,” *Phys. Rev. Lett.*, vol. 87, no. 24, p. 246802, Nov. 2001.
- [29] H. Kempa, H. . Semmelhack, P. Esquinazi, and Y. Kopelevich, “Absence of metal–insulator transition and coherent interlayer transport in oriented graphite in parallel magnetic fields,” *Solid State Commun.*, vol. 125, no. 1, pp. 1–5, Jan. 2003.
- [30] Y. Liu, W. S. Lew, and L. Sun, “Enhanced weak localization effect in few-layer graphene,” *Phys. Chem. Chem. Phys.*, vol. 13, no. 45, p. 20208, 2011.
- [31] X. Wu, X. Li, Z. Song, C. Berger, and W. A. de Heer, “Weak Antilocalization in Epitaxial Graphene: Evidence for Chiral Electrons,” *Phys. Rev. Lett.*, vol. 98, no. 13, p. 136801, Mar. 2007.
- [32] F. V. Tikhonenko, A. A. Kozikov, A. K. Savchenko, and R. V. Gorbachev, “Transition between Electron Localization and Antilocalization in Graphene,” *Phys. Rev. Lett.*, vol. 103, no. 22, p. 226801, Nov. 2009.

- [33] B. R. Matis, F. A. Bulat, A. L. Friedman, B. H. Houston, and J. W. Baldwin, "Giant negative magnetoresistance and a transition from strong to weak localization in hydrogenated graphene," *Phys. Rev. B*, vol. 85, no. 19, p. 195437, May 2012.
- [34] S. Pramanik, S. Bandyopadhyay, K. Garre, and M. Cahay, "Normal and inverse spin-valve effect in organic semiconductor nanowires and the background monotonic magnetoresistance," *Phys Rev B*, vol. 74, no. 23, p. 235329, Dec. 2006.
- [35] S. Bandyopadhyay and M. Cahay, *Introduction to Spintronics*, 1st ed. CRC Press, 2008.
- [36] E. Y. Tsymbal, A. Sokolov, I. F. Sabirianov, and B. Doudin, "Resonant Inversion of Tunneling Magnetoresistance," *Phys. Rev. Lett.*, vol. 90, no. 18, p. 186602, May 2003.
- [37] J. A. Katine, F. J. Albert, R. A. Buhrman, E. B. Myers, and D. C. Ralph, "Current-Driven Magnetization Reversal and Spin-Wave Excitations in Co/Cu/Co Pillars," *Phys. Rev. Lett.*, vol. 84, no. 14, pp. 3149–3152, Apr. 2000.
- [38] E. Cobas, A. L. Friedman, O. M. J. van't Erve, J. T. Robinson, and B. T. Jonker, "Graphene As a Tunnel Barrier: Graphene-Based Magnetic Tunnel Junctions," *Nano Lett.*, vol. 12, no. 6, pp. 3000–3004, Jun. 2012.
- [39] O. M. J. van 't Erve, A. L. Friedman, E. Cobas, C. H. Li, J. T. Robinson, and B. T. Jonker, "Low-resistance spin injection into silicon using graphene tunnel barriers," *Nat. Nanotechnol.*, vol. 7, no. 11, pp. 737–742, Nov. 2012.
- [40] G. Schmidt and L. W. Molenkamp, "Spin injection into semiconductors, physics and experiments," *Semicond. Sci. Technol.*, vol. 17, no. 4, p. 310, Apr. 2002.
- [41] B. Dlubak, M.-B. Martin, R. S. Weatherup, H. Yang, C. Deranlot, R. Blume, R. Schloegl, A. Fert, A. Anane, S. Hofmann, P. Seneor, and J. Robertson, "Graphene-Passivated Nickel as an Oxidation-Resistant Electrode for Spintronics," *ACS Nano*, vol. 6, no. 12, pp. 10930–10934, Dec. 2012.
- [42] K. Tsukagoshi, B. W. Alphenaar, and H. Ago, "Coherent transport of electron spin in a ferromagnetically contacted carbon nanotube," *Nature*, vol. 401, no. 6753, pp. 572–574, Oct. 1999.

- [43] B. Zhao, I. Mönch, H. Vinzelberg, T. Mühl, and C. M. Schneider, “Spin-coherent transport in ferromagnetically contacted carbon nanotubes,” *Appl. Phys. Lett.*, vol. 80, no. 17, pp. 3144–3146, Apr. 2002.
- [44] L. E. Hueso, J. M. Pruneda, V. Ferrari, G. Burnell, J. P. Valdés-Herrera, B. D. Simons, P. B. Littlewood, E. Artacho, A. Fert, and N. D. Mathur, “Transformation of spin information into large electrical signals using carbon nanotubes,” *Nature*, vol. 445, no. 7126, pp. 410–413, Jan. 2007.
- [45] D. Soriano, F. Muñoz-Rojas, J. Fernández-Rossier, and J. J. Palacios, “Hydrogenated graphene nanoribbons for spintronics,” *Phys. Rev. B*, vol. 81, no. 16, p. 165409, Apr. 2010.
- [46] A. L. Friedman, H. Chun, Y. J. Jung, D. Heiman, E. R. Glaser, and L. Menon, “Possible room-temperature ferromagnetism in hydrogenated carbon nanotubes,” *Phys. Rev. B*, vol. 81, no. 11, p. 115461, Mar. 2010.
- [47] S. Bodepudi, A. Singh, and S. Pramanik, “Current-Perpendicular-to-Plane Magnetoresistance in Chemical Vapor Deposition-Grown Multilayer Graphene,” *Electronics*, vol. 2, no. 3, pp. 315–331, Sep. 2013.
- [48] H. R. Shea, R. Martel, and P. Avouris, “Electrical Transport in Rings of Single-Wall Nanotubes: One-Dimensional Localization,” *Phys. Rev. Lett.*, vol. 84, no. 19, pp. 4441–4444, May 2000.
- [49] L. Langer, V. Bayot, E. Grivei, J.-P. Issi, J. P. Heremans, C. H. Olk, L. Stockman, C. Van Haesendonck, and Y. Bruynseraede, “Quantum Transport in a Multiwalled Carbon Nanotube,” *Phys. Rev. Lett.*, vol. 76, no. 3, pp. 479–482, Jan. 1996.
- [50] A. Bachtold, C. Strunk, J.-P. Salvetat, J.-M. Bonard, L. Forró, T. Nussbaumer, and C. Schönberger, “Aharonov–Bohm oscillations in carbon nanotubes,” *Nature*, vol. 397, no. 6721, pp. 673–675, Feb. 1999.
- [51] A. Fujiwara, K. Tomiyama, H. Suematsu, M. Yumura, and K. Uchida, “Quantum interference of electrons in multiwall carbon nanotubes,” *Phys. Rev. B*, vol. 60, no. 19, pp. 13492–13496, Nov. 1999.
- [52] G. Bergmann, “Weak localization in thin films: a time-of-flight experiment with conduction electrons,” *Phys. Rep.*, vol. 107, no. 1, pp. 1–58, May 1984.
- [53] P. A. Lee and T. V. Ramakrishnan, “Disordered electronic systems,” *Rev. Mod. Phys.*, vol. 57, no. 2, pp. 287–337, Apr. 1985.

- [54] M. Ohring, "Chapter 6 - Chemical Vapor Deposition," in *Materials Science of Thin Films (Second Edition)*, M. Ohring, Ed. San Diego: Academic Press, 2002, pp. 277–355.
- [55] K.-H. Dahmen, "Chemical Vapor Deposition," in *Encyclopedia of Physical Science and Technology (Third Edition)*, R. A. Meyers, Ed. New York: Academic Press, 2003, pp. 787–808.
- [56] S. A. Campbell, *The Science and Engineering of Microelectronic Fabrication*. New York: Oxford University Press, 2001.
- [57] S. A. Campbell, *Fabrication Engineering at the Micro- and Nanoscale*. 2013.
- [58] R. S. Edwards and K. S. Coleman, "Graphene synthesis: relationship to applications," *Nanoscale*, vol. 5, no. 1, pp. 38–51, Dec. 2012.
- [59] C. Mattevi, H. Kim, and M. Chhowalla, "A review of chemical vapour deposition of graphene on copper," *J. Mater. Chem.*, vol. 21, no. 10, pp. 3324–3334, Feb. 2011.
- [60] J.-C. Charlier and S. Iijima, "Growth Mechanisms of Carbon Nanotubes," in *Carbon Nanotubes*, M. S. Dresselhaus, G. Dresselhaus, and P. Avouris, Eds. Springer Berlin Heidelberg, 2001, pp. 55–81.
- [61] C. P. Deck and K. Vecchio, "Prediction of carbon nanotube growth success by the analysis of carbon–catalyst binary phase diagrams," *Carbon*, vol. 44, no. 2, pp. 267–275, Feb. 2006.
- [62] C. P. Deck and K. Vecchio, "Growth mechanism of vapor phase CVD-grown multi-walled carbon nanotubes," *Carbon*, vol. 43, no. 12, pp. 2608–2617, Oct. 2005.
- [63] M. Kumar, "Carbon Nanotube Synthesis and Growth Mechanism," in *Carbon Nanotubes - Synthesis, Characterization, Applications*, S. Yellampalli, Ed. InTech, 2011.
- [64] C. V. Raman & K. S. Krishnan, "A New Type of Secondary Radiation," *Nature*, vol. 121, pp. 501–502, Mar. 1928.
- [65] C. Casiraghi, A. Hartschuh, E. Lidorikis, H. Qian, H. Harutyunyan, T. Gokus, K. S. Novoselov, and A. C. Ferrari, "Rayleigh Imaging of Graphene and Graphene Layers," *Nano Lett.*, vol. 7, no. 9, pp. 2711–2717, Sep. 2007.

- [66] P. Blake, E. W. Hill, A. H. C. Neto, K. S. Novoselov, D. Jiang, R. Yang, T. J. Booth, and A. K. Geim, “Making graphene visible,” *Appl. Phys. Lett.*, vol. 91, no. 6, p. 063124, Aug. 2007.
- [67] A. C. Ferrari and D. M. Basko, “Raman spectroscopy as a versatile tool for studying the properties of graphene,” *Nat. Nanotechnol.*, vol. 8, no. 4, pp. 235–246, Apr. 2013.
- [68] C. Kittel, *Introduction to solid state physics*. Hoboken, NJ: Wiley, 2005.
- [69] P. Y. Yu and M. Cardona, *Fundamentals of Semiconductors: Physics and Materials Properties*. Berlin; New York: Springer, 2010.
- [70] T. R. Hart, R. L. Aggarwal, and B. Lax, “Temperature Dependence of Raman Scattering in Silicon,” *Phys. Rev. B*, vol. 1, no. 2, pp. 638–642, Jan. 1970.
- [71] M. F. L. D. Volder, S. H. Tawfick, R. H. Baughman, and A. J. Hart, “Carbon Nanotubes: Present and Future Commercial Applications,” *Science*, vol. 339, no. 6119, pp. 535–539, Feb. 2013.
- [72] D. Sun, M. Y. Timmermans, Y. Tian, A. G. Nasibulin, E. I. Kauppinen, S. Kishimoto, T. Mizutani, and Y. Ohno, “Flexible high-performance carbon nanotube integrated circuits,” *Nat. Nanotechnol.*, vol. 6, no. 3, pp. 156–161, Mar. 2011.
- [73] T. Rueckes, K. Kim, E. Joselevich, G. Y. Tseng, C.-L. Cheung, and C. M. Lieber, “Carbon Nanotube-Based Nonvolatile Random Access Memory for Molecular Computing,” *Science*, vol. 289, no. 5476, pp. 94–97, Jul. 2000.
- [74] M. H. van der Veen, B. Vereecke, M. Sugiura, Y. Kashiwagi, X. Ke, D. J. Cott, J. K. M. Vanpaemel, P. M. Vereecken, S. De Gendt, C. Huyghebaert, and Z. Tokei, “Electrical and structural characterization of 150 nm CNT contacts with Cu damascene top metallization,” in *Interconnect Technology Conference (ITC), 2012 IEEE International*, 2012, pp. 1–3.
- [75] S. W. Hong, F. Du, W. Lan, S. Kim, H.-S. Kim, and J. A. Rogers, “Monolithic Integration of Arrays of Single-Walled Carbon Nanotubes and Sheets of Graphene,” *Adv. Mater.*, vol. 23, no. 33, pp. 3821–3826, 2011.
- [76] N. Tombros, C. Jozsa, M. Popinciuc, H. T. Jonkman, and B. J. van Wees, “Electronic spin transport and spin precession in single graphene layers at room temperature,” *Nature*, vol. 448, no. 7153, pp. 571–574, Aug. 2007.
- [77] Y. W. Son, M. L. Cohen, and S. G. Louie, “Half-metallic graphene nanoribbons,” *Nature*, vol. 444, no. 7117, pp. 347–349, Nov. 2006.

- [78] R. R. Nair, P. Blake, A. N. Grigorenko, K. S. Novoselov, T. J. Booth, T. Stauber, N. M. R. Peres, and A. K. Geim, “Fine Structure Constant Defines Visual Transparency of Graphene,” *Science*, vol. 320, no. 5881, pp. 1308–1308, Jun. 2008.
- [79] Z. Q. Li, E. A. Henriksen, Z. Jiang, Z. Hao, M. C. Martin, P. Kim, H. L. Stormer, and D. N. Basov, “Dirac charge dynamics in graphene by infrared spectroscopy,” *Nat. Phys.*, vol. 4, no. 7, pp. 532–535, Jul. 2008.
- [80] C. Berger, Z. Song, T. Li, X. Li, A. Y. Ogbazghi, R. Feng, Z. Dai, A. N. Marchenkov, E. H. Conrad, P. N. First, and W. A. de Heer, “Ultrathin Epitaxial Graphite: 2D Electron Gas Properties and a Route toward Graphene-based Nanoelectronics,” *J. Phys. Chem. B*, vol. 108, no. 52, pp. 19912–19916, Dec. 2004.
- [81] S. Bae, H. Kim, Y. Lee, X. Xu, J.-S. Park, Y. Zheng, J. Balakrishnan, T. Lei, H. Ri Kim, Y. I. Song, Y.-J. Kim, K. S. Kim, B. Özyilmaz, J.-H. Ahn, B. H. Hong, and S. Iijima, “Roll-to-roll production of 30-inch graphene films for transparent electrodes,” *Nat. Nanotechnol.*, vol. 5, no. 8, pp. 574–578, Aug. 2010.
- [82] C. Lee, X. Wei, J. W. Kysar, and J. Hone, “Measurement of the Elastic Properties and Intrinsic Strength of Monolayer Graphene,” *Science*, vol. 321, no. 5887, pp. 385–388, Jul. 2008.
- [83] T. R. Nayak, H. Andersen, V. S. Makam, C. Khaw, S. Bae, X. Xu, P.-L. R. Ee, J.-H. Ahn, B. H. Hong, G. Pastorin, and B. Özyilmaz, “Graphene for Controlled and Accelerated Osteogenic Differentiation of Human Mesenchymal Stem Cells,” *ACS Nano*, vol. 5, no. 6, pp. 4670–4678, Jun. 2011.
- [84] S. S. P. Parkin, “Applications of Magnetic Nanostructures,” in *Spin Dependent Transport in Magnetic Nanostructures*, vol. 3, 1 vols., T. Shinjo and S. Maekawa, Eds. CRC Press, 2002.
- [85] S. Frank, P. Poncharal, Z. L. Wang, and W. A. de Heer, “Carbon Nanotube Quantum Resistors,” *Science*, vol. 280, no. 5370, pp. 1744–1746, Jun. 1998.
- [86] J.-H. Park, E. Vescovo, H.-J. Kim, C. Kwon, R. Ramesh, and T. Venkatesan, “Direct evidence for a half-metallic ferromagnet,” *Nature*, vol. 392, no. 6678, pp. 794–796, Apr. 1998.
- [87] M. Bowen, M. Bibes, A. Barthélémy, J.-P. Contour, A. Anane, Y. Lemaître, and A. Fert, “Nearly total spin polarization in La<sub>2</sub>/3Sr<sub>1</sub>/3MnO<sub>3</sub>

- from tunneling experiments,” *Appl. Phys. Lett.*, vol. 82, no. 2, pp. 233–235, Jan. 2003.
- [88] M. B. Murphey, J. D. Bergeson, S. J. Etzkorn, L. Qu, L. Li, L. Dai, and A. J. Epstein, “Spin-valve behavior in porous alumina-embedded carbon nanotube array with cobalt nanoparticle spin injectors,” *Synth. Met.*, vol. 160, no. 3–4, pp. 235–237, Feb. 2010.
- [89] X. Hoffer, C. Klinke, J.-M. Bonard, L. Gravier, and J.-E. Wegrowe, “Spin-dependent magnetoresistance in multiwall carbon nanotubes,” *EPL Europhys. Lett.*, vol. 67, no. 1, p. 103, Jul. 2004.
- [90] J. D. Bergeson, S. J. Etzkorn, M. B. Murphey, L. Qu, J. Yang, L. Dai, and A. J. Epstein, “Iron nanoparticle driven spin-valve behavior in aligned carbon nanotube arrays,” *Appl. Phys. Lett.*, vol. 93, no. 17, p. 172505, Oct. 2008.
- [91] V. M. Karpan, P. A. Khomyakov, A. A. Starikov, G. Giovannetti, M. Zwierzycki, M. Talanana, G. Brocks, J. van den Brink, and P. J. Kelly, “Theoretical prediction of perfect spin filtering at interfaces between close-packed surfaces of Ni or Co and graphite or graphene,” *Phys. Rev. B*, vol. 78, no. 19, p. 195419, Nov. 2008.
- [92] V. M. Karpan, G. Giovannetti, P. A. Khomyakov, M. Talanana, A. A. Starikov, M. Zwierzycki, J. van den Brink, G. Brocks, and P. J. Kelly, “Graphite and Graphene as Perfect Spin Filters,” *Phys. Rev. Lett.*, vol. 99, no. 17, p. 176602, Oct. 2007.
- [93] K. S. Novoselov, D. Jiang, F. Schedin, T. J. Booth, V. V. Khotkevich, S. V. Morozov, and A. K. Geim, “Two-dimensional atomic crystals,” *Proc. Natl. Acad. Sci. U. S. A.*, vol. 102, no. 30, pp. 10451–10453, Jul. 2005.
- [94] X. Zhang and Y. Xie, “Recent advances in free-standing two-dimensional crystals with atomic thickness: design, assembly and transfer strategies,” *Chem. Soc. Rev.*, vol. 42, no. 21, pp. 8187–8199, Oct. 2013.
- [95] K. S. Novoselov and A. H. C. Neto, “Two-dimensional crystals-based heterostructures: materials with tailored properties,” *Phys. Scr.*, vol. 2012, no. T146, p. 014006, Jan. 2012.
- [96] M. J. Allen, V. C. Tung, and R. B. Kaner, “Honeycomb Carbon: A Review of Graphene,” *Chem. Rev.*, vol. 110, no. 1, pp. 132–145, Jan. 2010.
- [97] J. H. Warner, F. Schäffel, A. Bachmatiuk, and M. H. Rummeli, “Chapter 4 - Methods for Obtaining Graphene,” in *Graphene*, J. H. Warner, F.

- Schäffel, A. Bachmatiuk, and M. H. Rummeli, Eds. Elsevier, 2013, pp. 129–228.
- [98] K. S. Novoselov, A. K. Geim, S. V. Morozov, D. Jiang, Y. Zhang, S. V. Dubonos, I. V. Grigorieva, and A. A. Firsov, “Electric Field Effect in Atomically Thin Carbon Films,” *Science*, vol. 306, no. 5696, pp. 666–669, Oct. 2004.
- [99] Y. Hernandez, V. Nicolosi, M. Lotya, F. M. Blighe, Z. Sun, S. De, I. T. McGovern, B. Holland, M. Byrne, Y. K. Gun’Ko, J. J. Boland, P. Niraj, G. Duesberg, S. Krishnamurthy, R. Goodhue, J. Hutchison, V. Scardaci, A. C. Ferrari, and J. N. Coleman, “High-yield production of graphene by liquid-phase exfoliation of graphite,” *Nat. Nanotechnol.*, vol. 3, no. 9, pp. 563–568, Sep. 2008.
- [100] J. Zhu, “Graphene production: New solutions to a new problem,” *Nat. Nanotechnol.*, vol. 3, no. 9, pp. 528–529, Sep. 2008.
- [101] W. Zhao, M. Fang, F. Wu, H. Wu, L. Wang, and G. Chen, “Preparation of graphene by exfoliation of graphite using wet ball milling,” *J. Mater. Chem.*, vol. 20, no. 28, pp. 5817–5819, Jul. 2010.
- [102] S. Niyogi, E. Bekyarova, M. E. Itkis, J. L. McWilliams, M. A. Hamon, and R. C. Haddon, “Solution Properties of Graphite and Graphene,” *J. Am. Chem. Soc.*, vol. 128, no. 24, pp. 7720–7721, Jun. 2006.
- [103] J. S. Choi, J.-S. Kim, I.-S. Byun, D. H. Lee, M. J. Lee, B. H. Park, C. Lee, D. Yoon, H. Cheong, K. H. Lee, Y.-W. Son, J. Y. Park, and M. Salmeron, “Friction Anisotropy–Driven Domain Imaging on Exfoliated Monolayer Graphene,” *Science*, vol. 333, no. 6042, pp. 607–610, Jul. 2011.
- [104] A. Reina, X. Jia, J. Ho, D. Nezich, H. Son, V. Bulovic, M. S. Dresselhaus, and J. Kong, “Large Area, Few-Layer Graphene Films on Arbitrary Substrates by Chemical Vapor Deposition,” *Nano Lett.*, vol. 9, no. 1, pp. 30–35, Jan. 2009.
- [105] X. Li, W. Cai, J. An, S. Kim, J. Nah, D. Yang, R. Piner, A. Velamakanni, I. Jung, E. Tutuc, S. K. Banerjee, L. Colombo, and R. S. Ruoff, “Large-Area Synthesis of High-Quality and Uniform Graphene Films on Copper Foils,” *Science*, vol. 324, no. 5932, pp. 1312–1314, Jun. 2009.
- [106] Y. S. Dedkov, M. Fonin, U. Rüdiger, and C. Laubschat, “Rashba Effect in the Graphene/Ni(111) System,” *Phys. Rev. Lett.*, vol. 100, no. 10, p. 107602, Mar. 2008.

- [107] J. Wintterlin and M.-L. Bocquet, “Graphene on metal surfaces,” *Surf. Sci.*, vol. 603, no. 10–12, pp. 1841–1852, Jun. 2009.
- [108] C. Gong, G. Lee, B. Shan, E. M. Vogel, R. M. Wallace, and K. Cho, “First-principles study of metal–graphene interfaces,” *J. Appl. Phys.*, vol. 108, no. 12, p. 123711, Dec. 2010.
- [109] G. Giovannetti, P. A. Khomyakov, G. Brocks, V. M. Karpan, J. van den Brink, and P. J. Kelly, “Doping Graphene with Metal Contacts,” *Phys. Rev. Lett.*, vol. 101, no. 2, p. 026803, Jul. 2008.
- [110] Z. Xu and M. J. Buehler, “Interface structure and mechanics between graphene and metal substrates: a first-principles study,” *J. Phys. Condens. Matter*, vol. 22, no. 48, p. 485301, Dec. 2010.
- [111] Y. S. Dedkov and M. Fonin, “Electronic and magnetic properties of the graphene–ferromagnet interface,” *New J. Phys.*, vol. 12, no. 12, p. 125004, Dec. 2010.
- [112] Y. S. Dedkov, A. Generalov, E. N. Voloshina, and M. Fonin, “Structural and electronic properties of Fe<sub>3</sub>O<sub>4</sub>/graphene/Ni(111) junctions,” *Phys. Status Solidi RRL – Rapid Res. Lett.*, vol. 5, no. 7, pp. 226–228, 2011.
- [113] S. M. Wang, Y. H. Pei, X. Wang, H. Wang, Q. N. Meng, H. W. Tian, X. L. Zheng, W. T. Zheng, and Y. C. Liu, “Synthesis of graphene on a polycrystalline Co film by radio-frequency plasma-enhanced chemical vapour deposition,” *J. Phys. Appl. Phys.*, vol. 43, no. 45, p. 455402, Nov. 2010.
- [114] N. Zhan, G. Wang, and J. Liu, “Cobalt-assisted large-area epitaxial graphene growth in thermal cracker enhanced gas source molecular beam epitaxy,” *Appl. Phys. A*, vol. 105, no. 2, pp. 341–345, Nov. 2011.
- [115] M. E. Ramón, A. Gupta, C. Corbet, D. A. Ferrer, H. C. P. Movva, G. Carpenter, L. Colombo, G. Bourianoff, M. Doczy, D. Akinwande, E. Tutuc, and S. K. Banerjee, “CMOS-Compatible Synthesis of Large-Area, High-Mobility Graphene by Chemical Vapor Deposition of Acetylene on Cobalt Thin Films,” *ACS Nano*, vol. 5, no. 9, pp. 7198–7204, Sep. 2011.
- [116] C. M. Orofeo, H. Ago, B. Hu, and M. Tsuji, “Synthesis of large area, homogeneous, single layer graphene films by annealing amorphous carbon on Co and Ni,” *Nano Res.*, vol. 4, no. 6, pp. 531–540, Jun. 2011.
- [117] H. Ago, Y. Ito, N. Mizuta, K. Yoshida, B. Hu, C. M. Orofeo, M. Tsuji, K. Ikeda, and S. Mizuno, “Epitaxial Chemical Vapor Deposition Growth of

Single-Layer Graphene over Cobalt Film Crystallized on Sapphire,” *ACS Nano*, vol. 4, no. 12, pp. 7407–7414, Dec. 2010.

- [118] N. K. Memon, S. D. Tse, M. Chhowalla, and B. H. Kear, “Role of substrate, temperature, and hydrogen on the flame synthesis of graphene films,” *Proc. Combust. Inst.*, vol. 34, no. 2, pp. 2163–2170, 2013.
- [119] R. S. Edwards and K. S. Coleman, “Graphene Film Growth on Polycrystalline Metals,” *Acc. Chem. Res.*, vol. 46, no. 1, pp. 23–30, Jan. 2013.
- [120] M. Zheng, K. Takei, B. Hsia, H. Fang, X. Zhang, N. Ferralis, H. Ko, Y.-L. Chueh, Y. Zhang, R. Maboudian, and A. Javey, “Metal-catalyzed crystallization of amorphous carbon to graphene,” *Appl. Phys. Lett.*, vol. 96, no. 6, pp. 063110–063110–3, Feb. 2010.
- [121] Q. Yu, J. Lian, S. Siriponglert, H. Li, Y. P. Chen, and S.-S. Pei, “Graphene segregated on Ni surfaces and transferred to insulators,” *Appl. Phys. Lett.*, vol. 93, no. 11, p. 113103, Sep. 2008.
- [122] K. S. Kim, Y. Zhao, H. Jang, S. Y. Lee, J. M. Kim, K. S. Kim, J.-H. Ahn, P. Kim, J.-Y. Choi, and B. H. Hong, “Large-scale pattern growth of graphene films for stretchable transparent electrodes,” *Nature*, vol. 457, no. 7230, pp. 706–710, Feb. 2009.
- [123] Q. Yu, J. Lian, S. Siriponglert, H. Li, Y. P. Chen, and S.-S. Pei, “Graphene segregated on Ni surfaces and transferred to insulators,” *Appl. Phys. Lett.*, vol. 93, no. 11, pp. 113103–113103–3, Sep. 2008.
- [124] J. Berashevich and T. Chakraborty, “Interlayer repulsion and decoupling effects in stacked turbostratic graphene flakes,” *Phys. Rev. B*, vol. 84, no. 3, p. 033403, Jul. 2011.
- [125] L. M. Malard, M. A. Pimenta, G. Dresselhaus, and M. S. Dresselhaus, “Raman spectroscopy in graphene,” *Phys. Rep.*, vol. 473, no. 5–6, pp. 51–87, Apr. 2009.
- [126] C. Faugeras, A. Nerrière, M. Potemski, A. Mahmood, E. Dujardin, C. Berger, and W. A. de Heer, “Few-layer graphene on SiC, pyrolytic graphite, and graphene: A Raman scattering study,” *Appl. Phys. Lett.*, vol. 92, no. 1, p. 011914, Jan. 2008.
- [127] D. R. Lenski and M. S. Fuhrer, “Raman and optical characterization of multilayer turbostratic graphene grown via chemical vapor deposition,” *J. Appl. Phys.*, vol. 110, no. 1, p. 013720, Jul. 2011.

- [128] A. Reina and J. Kong, “Graphene Growth by CVD Methods,” in *Graphene Nanoelectronics*, R. Murali, Ed. Springer US, 2012, pp. 167–203.
- [129] J. Lahiri, Y. Lin, P. Bozkurt, I. I. Oleynik, and M. Batzill, “An extended defect in graphene as a metallic wire,” *Nat. Nanotechnol.*, vol. 5, no. 5, pp. 326–329, May 2010.
- [130] T. Osada, “Negative Interlayer Magnetoresistance and Zero-Mode Landau Level in Multilayer Dirac Electron Systems,” *J. Phys. Soc. Jpn.*, vol. 77, no. 8, p. 084711, 2008.
- [131] T. Morinari and T. Tohyama, “Crossover from Positive to Negative Interlayer Magnetoresistance in Multilayer Massless Dirac Fermion System with Non-Vertical Interlayer Tunneling,” *J. Phys. Soc. Jpn.*, vol. 79, no. 4, p. 044708, 2010.
- [132] N. Tajima, S. Sugawara, R. Kato, Y. Nishio, and K. Kajita, “Effect of the Zero-Mode Landau Level on Interlayer Magnetoresistance in Multilayer Massless Dirac Fermion Systems,” *Phys. Rev. Lett.*, vol. 102, no. 17, p. 176403, Apr. 2009.
- [133] N. Tajima, M. Sato, S. Sugawara, R. Kato, Y. Nishio, and K. Kajita, “Spin and valley splittings in multilayered massless Dirac fermion system,” *Phys. Rev. B*, vol. 82, no. 12, p. 121420, Sep. 2010.
- [134] J. Heo, H. J. Chung, S.-H. Lee, H. Yang, D. H. Seo, J. K. Shin, U.-I. Chung, S. Seo, E. H. Hwang, and S. Das Sarma, “Nonmonotonic temperature dependent transport in graphene grown by chemical vapor deposition,” *Phys. Rev. B*, vol. 84, no. 3, p. 035421, Jul. 2011.
- [135] W. Kang, T. Osada, Y. J. Jo, and H. Kang, “Interlayer Magnetoresistance of Quasi-One-Dimensional Layered Organic Conductors,” *Phys. Rev. Lett.*, vol. 99, no. 1, p. 017002, Jul. 2007.
- [136] M. Assili and S. Haddad, “Interlayer magnetoresistance in multilayer Dirac electron systems: motion and merging of Dirac cones,” *J. Phys. Condens. Matter*, vol. 25, no. 36, p. 365503, Sep. 2013.
- [137] A. P. Singh, S. C. Bodepudi, K. Alam, and S. Pramanik, “High Density Integration of Carbon Nanotube Spin Valves,” in *2011 International Conference on Nanoscience, Technology and Societal Implications (NSTSI)*, 2011, pp. 1–4.
- [138] J. Åkerman, “Toward a Universal Memory,” *Science*, vol. 308, no. 5721, pp. 508–510, Apr. 2005.

- [139] K. Tsukagoshi, B. W. Alphenaar, and H. Ago, "Coherent transport of electron spin in a ferromagnetically contacted carbon nanotube," *Nature*, vol. 401, no. 6753, pp. 572–574, Oct. 1999.
- [140] B. Zhao, I. Monch, H. Vinzelberg, T. Muhl, and C. M. Schneider, "Spin-coherent transport in ferromagnetically contacted carbon nanotubes," *Appl. Phys. Lett.*, vol. 80, no. 17, pp. 3144–3146, 2002.
- [141] L. E. Hueso, J. M. Pruneda, V. Ferrari, G. Burnell, J. P. Valdes-Herrera, B. D. Simons, P. B. Littlewood, E. Artacho, A. Fert, and N. D. Mathur, "Transformation of spin information into large electrical signals using carbon nanotubes," *Nature*, vol. 445, no. 7126, pp. 410–413, 2007.
- [142] M. B. Murphey, J. D. Bergeson, S. J. Etzkorn, L. Qu, L. Li, L. Dai, and A. J. Epstein, "Spin-valve behavior in porous alumina-embedded carbon nanotube array with cobalt nanoparticle spin injectors," *Synth. Met.*, vol. 160, no. 3–4, pp. 235–237, Feb. 2010.
- [143] K. M. Alam, A. P. Singh, S. C. Bodepudi, and S. Pramanik, "Fabrication of hexagonally ordered nanopores in anodic alumina: An alternative pretreatment," *Surf. Sci.*, vol. 605, no. 3–4, pp. 441–449, Feb. 2011.
- [144] S.-H. Jeong, H.-Y. Hwang, K.-H. Lee, and Y. Jeong, "Template-based carbon nanotubes and their application to a field emitter," *Appl. Phys. Lett.*, vol. 78, no. 14, pp. 2052–2054, Apr. 2001.
- [145] L. Dai, P. Wang, and K. Bosnick, "Large-scale production and metrology of vertically aligned carbon nanotube films," *J. Vac. Sci. Technol. Vac. Surf. Films*, vol. 27, no. 4, p. 1071, 2009.
- [146] K. Bosnick and L. Dai, "Growth Kinetics in a Large-Bore Vertically Aligned Carbon Nanotube Film Deposition Process," *J. Phys. Chem. C*, vol. 114, pp. 7226–7230, 2010.
- [147] S.-H. Jeong, O.-J. Lee, K.-H. Lee, S. H. Oh, and C.-G. Park, "Preparation of Aligned Carbon Nanotubes with Prescribed Dimensions: Template Synthesis and Sonication Cutting Approach," *Chem. Mater.*, vol. 14, no. 4, pp. 1859–1862, 2002.
- [148] Y. S. Shin, J. H. Yang, C.-Y. Park, M. H. Kwon, J.-B. Yoo, and C. W. Yang, "Synthesis of Crystalline Carbon Nanotube Arrays on Anodic Aluminum Oxide Using Catalyst Reduction with Low Pressure Thermal Chemical Vapor Deposition," *Jpn. J. Appl. Phys.*, vol. 45, no. No. 3A, pp. 1869–1872, 2006.

- [149] I. Žutić and S. Das Sarma, “Spintronics: Fundamentals and applications,” *Rev. Mod. Phys.*, vol. 76, no. 2, pp. 323–410, Apr. 2004.
- [150] M. Julliere, “Tunneling between ferromagnetic films,” *Phys. Lett. A*, vol. 54, no. 3, pp. 225–226, Sep. 1975.
- [151] Z. H. Xiong, D. Wu, Z. Vally Vardeny, and J. Shi, “Giant magnetoresistance in organic spin-valves,” *Nature*, vol. 427, no. 6977, pp. 821–824, Feb. 2004.
- [152] G. S. Diniz, A. Latgé, and S. E. Ulloa, “Helicoidal Fields and Spin Polarized Currents in Carbon Nanotube–DNA Hybrids,” *Phys. Rev. Lett.*, vol. 108, no. 12, p. 126601, Mar. 2012.